Bulletin of the Seismological Society of America, Vol. 98, No. 3, pp. 1186–1206, June 2008, doi: 10.1785/0120070190

Scale-Model and Numerical Simulations of Near-Fault Seismic Directivity

by Steven M. Day, Sarah H. Gonzalez, Rasool Anooshehpoor, and James N. Brune

Abstract Foam rubber experiments simulating unilaterally propagating strike-slip earthquakes provide a means to explore the sensitivity of near-fault ground motions to rupture geometry. Subsurface accelerometers on the model fault plane show rupture propagation that approaches a limiting velocity close to the Rayleigh velocity. The slip-velocity waveform at depth is cracklike (slip duration of the order of narrower fault dimension W divided by S-wave speed β). Surface accelerometers record near-fault ground motion enhanced along strike by rupture-induced directivity. Most experimental features (initiation time, shape, duration and absolute amplitude of acceleration pulses) are successfully reproduced by a 3D spontaneous-rupture numerical model of the experiments. Numerical- and experimental-model acceleration pulses show similar decay with distance away from the fault, and fault-normal components in both models show similar, large amplitude growth with distance along fault strike. This forward directivity effect is also evident in response spectra: the fault-normal spectral response peak (at period $\sim W/3\beta$) increases approximately sixfold along strike, on average, in the experiments, with similar increase (about fivefold) in the corresponding numerical simulation. The experimental- and numerical-model response spectra agree with an empirical directivity model for natural earthquakes at long periods (near $\sim W/\beta$), and both overpredict shorter-period empirical directivity effects, with the amount of overprediction increasing systematically with diminishing period. We attribute this difference to rupture- and wavefront incoherence in natural earthquakes, due to fault-zone heterogeneities in stress, frictional resistance, and elastic properties present in the Earth but absent or minimal in the experimental and numerical models. Rupture-front incoherence is an important component of source models for ground-motion prediction, but finding an effective kinematic parameterization may be challenging.

Introduction

We analyze acceleration records from scale-model earthquake experiments, together with those from numerical simulations of those experiments, in an effort to gain improved understanding of near-fault strong ground motion from shallow, strike-slip earthquakes. By near fault, we refer to sites whose distance from the surface trace of the rupture is bounded by roughly the seismogenic depth (e.g., roughly 15 km for faults in the western United States). In that regime, ground-motion amplitudes may be strongly enhanced, relative to more distant sites.

The high intensity and damage potential of near-fault ground motion is due both to the proximity of the source and to the occurrence of pronounced directivity effects (e.g., Somerville *et al.*, 1997). Directivity refers to the intensification of ground motion at sites whose direction from the hypocenter forms a small angle with the predominant rupture propagation direction (and diminution at corresponding supplementary angles). Directivity-enhanced strong motion near the surface trace of large earthquake ruptures is frequently pulselike in waveform. That is, most of the ground displacement takes place in a coherent, high-velocity (sometimes exceeding 1 m/sec) pulse of short duration (typically 2–4 sec), with the strongest motion usually polarized in the direction perpendicular to the fault (e.g., Archuleta and Hartzell, 1981; Anderson and Bertero, 1987; Hall *et al.*, 1995). Such pulses can be highly damaging to structures, and because of the nonlinearity of structural response to high-amplitude ground motion, reliable modeling of the performance of a particular structure may require constraints on the pulse waveform, as well as estimates of its amplitude and duration (Hall *et al.*, 1995).

A number of factors place limits on our current understanding of the physics of the earthquake rupture process, and therefore on our ability to reliably quantify near-fault

ground motion for use in engineering studies. One factor is the difficulty of obtaining measurements of the driving (tectonic) and resisting (frictional) stresses in the source region. A second is the paucity of strong ground motion data from large earthquakes recorded within the near-fault region (i.e., within a horizontal distance roughly equal to the seismogenic depth). Further limiting our understanding of rupture physics is the inaccessibility to seismic instrumentation of the seismogenic zone at depth.

Foam rubber earthquake experiments provide a means to explore the sensitivity of near-fault ground motion to fault and rupture geometry, offering insights that would be difficult to achieve from the limited recordings available in the near-fault region of large natural earthquakes (Brune and Anooshehpoor, 1998; Day and Ely, 2002). Among the advantages offered by foam rubber earthquake experiments are that the bulk and fault-surface physical properties of the model, and its stress state prior to rupture, can be measured independently of the ground motion. Additionally, the experiments can provide more complete recordings of ground motion (including subsurface recordings) than are available for real earthquakes, and the foam modeling also offers some degree of experimental repeatability.

In this study, we analyze a large set (43 events) of scale-model earthquakes induced in a foam rubber model, and numerically simulate representative events using a 3D finite difference method (Day, 1982b; Day and Ely, 2002; Day *et al.*, 2005). This combined approach is motivated by evidence (Day and Ely, 2002) that experimental and numerical earthquake models complement each other in a number of respects and that the combined approach therefore provides a valuable cross validation that can increase our understanding of, and confidence in, the modeling results. For example, numerical simulations have the potential to reveal the presence of unexpected artifacts attributable to the experimental configuration, such as artificial effects induced by the model boundaries, loading apparatus, or sensor emplacement. Conversely, experiments have the potential to reveal important consequences of some of the highly simplified physical assumptions we have made in the construction of the numerical model, such as the mode of event nucleation and the friction law parameterization. Likewise, satisfactory agreement between experimental and numerical results may constitute valuable corroboration of the theoretical and computational soundness of the numerical modeling method.

The next two sections of the paper briefly describe the foam rubber and numerical models, respectively. These sections are followed by a dimensional analysis of the problem, showing that, with some appropriate simplifications, the theoretical earthquake model underlying the numerical simulations can be characterized by four dimensionless quantities. The experimental results are then described. Because a key objective is the quantification of directivity effects, considerable attention is given to characterizing the style and velocity of rupture, as well as the dependence of the acceleration levels on station location relative to the rupture initiation point. We then present some numerical simulations of the experiments, constrained in considerable degree by independently measured model parameters. The numerical-model accelerograms mimic the main qualitative features of the experimental accelerograms. They show quantitative agreement with the amplitude, period, and timing of the main experimental phases, to within roughly their level of experimental repeatability. The simulations also reveal some trade-offs among the more poorly constrained model parameters. With the aid of the simulation results, we summarize the key dimensionless ratios of the model and compare those with comparable estimates for natural earthquakes.

We then examine directivity effects. To facilitate comparison with the empirical study of natural earthquakes by Somerville *et al.* (1997), we analyze response spectra. We perform a regression analysis of response-spectral ordinates from both the foam rubber experiments and a numerical simulation, using the parameterization proposed in the Somerville *et al.* study.

Foam Rubber Model

Model Geometry and Loading Scheme

A foam rubber model is used to simulate unilaterally propagating strike-slip earthquakes. The model consists of two stacked blocks of foam. The dimensions of each block are $0.95 \times 1.83 \times 2.0$ m. The interface between the upper and lower blocks represents a fault plane, and the total area of the fault plane is 3.66 m^2. The bottom of the lower block remains fixed to the floor, while the upper block is driven horizontally over the lower block by a hydraulic piston mounted to the wall. The motion of the upper block over the lower block produces stick-slip events over the interface (or fault plane) between the blocks. A total of 43 individual stick-slip events having similar hypocenter locations are used to study the effects of directivity on near-fault ground motion.

Figure 1 shows the foam model diagrammatically. The bottom of the lower foam block is attached to a plywood sheet that is anchored to a concrete floor (Brune and Anooshehpoor, 1998). Similarly, the top of the upper block is attached to a plywood sheet that is secured to a rigid frame. Thin plywood sheets are also attached to the sides of both blocks. The only fully free boundaries are the front and back of the blocks; the front surface is intended to represent the earth's free surface, so this arrangement models vertical, strike-slip faulting. The upper block and attached rigid frame are supported by four steel pipes equipped with scaffolding jacks and guiding rollers at each corner (Brune and Anooshehpoor, 1998).

Stress Conditions

By adjusting the four jacks, it is possible to control the magnitude of the normal force on the fault plane. The initial normal stress (we will cite compressive stress values, $-\sigma_n$,

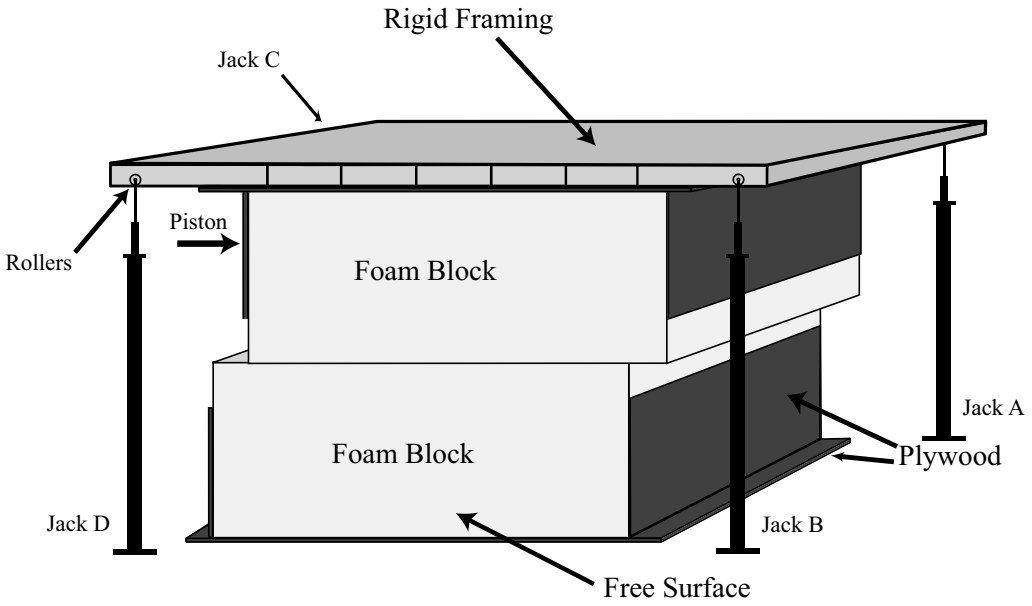

Figure 1. Sketch of the foam rubber model. Each of the two blocks has dimensions $0.95 \times 1.83 \times 2.0$ m. The front surface represents the free surface, so this arrangement models vertical, strike-slip faulting.

σ_n being positive in tension) was set to 320 Pa for most of the experiments used in this study. Several additional experiments were done with the initial normal stress equal to 385 and 538 Pa, respectively. Shear force is provided by the hydraulic piston, which has a constant driving velocity of 1 mm/sec.

In order to confine slip to a shallow, high-aspect-ratio rupture surface, the initial shear stress on the lower portion of the fault plane (i.e., the portion furthest from the model free surface) is artificially reduced, relative to that of the upper portion. The shear load on the entire model is first raised to the point of failure, while a uniform normal load is maintained. Then the two rear jacks (A and C in Fig. 1) are raised to reduce the normal stresses on the lower portion of the fault. The gradient in normal stress results in a relaxation of the shear stress through stable sliding on the lower portion, with transference of the shear load to the upper portion. Then jacks A and C are lowered so that the normal stress is again uniform and sufficiently high to relock the fault. Numerical simulations indicate that this method of lowering the shear stress on the lower portion is sufficient to keep it completely locked during a stick-slip event on the upper portion. This is confirmed by direct measurements of fault slip in an experiment in which fault-plane sensors are present on the lower portion. We estimate that roughly the lower one-half of the fault is kept locked by this scheme, but there is considerable uncertainty about the locking depth.

It is difficult to estimate the pre- and postevent shear-stress levels (on the active, upper portion of the fault) following this loading process, because of uncertainties in the fraction of the fault area that is locked as well as in the amount of stress reduction on the lower portion when the rear jacks are raised. We instead examine separate experiments in which the entire fault surface is loaded to failure, with the shearing load measured just before and after a stick-slip event (which slips the whole fault in this case). Figure 2 shows the pre- and postevent average shear stress, as a function of normal stress. The data points and error bars show averages and standard deviations (from at least 10 events at each normal-stress level). The mean preevent shear stresses (τ_0) at the same three normal-stress levels (i.e., $\sigma_n = 320$, 385, and 538 Pa) are 457, 507, and 668 Pa, respectively, with roughly 4% standard deviations.

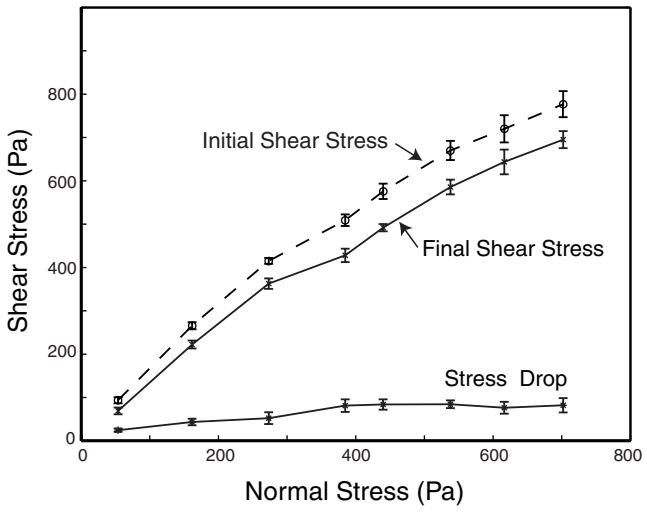

Figure 2. Pre- and postevent average shear stress, as a function of normal stress, for experiments in which the entire fault surface is loaded to failure. The data points and error bars show averages and standard deviations (from at least 10 events at each normal-stress level).

Bulk and Surface Properties

We make the assumption that friction on the foam surface, whatever its true microscale origins, can be reasonably parameterized in terms of static and dynamic friction coefficients. We take the ratio of final shear stress to normal stress in Figure 2 as our estimate of the dynamic friction coefficient, which then has a weak dependence on normal stress. For the three normal-stress levels used in this study, we find means of (interpolating in the 320 Pa normal-stress case) $\mu_d(320) = 1.22$, $\mu_d(385) = 1.11$, and $\mu_d(538) = 1.09$, with uncertainties of roughly 4% in each case. On the notion that rupture nucleates at local inhomogeneities where the ratio of shear to normal stress is higher than average, we assume the existence of a static coefficient μ_s higher than the ratio τ_0/σ_n given in Figure 2, because those shear-stress values are fault-plane averages (i.e., just the ratio of total shear load to fault area).

The foam density is 16 kg/m^3. We measured the *P*- and *S*-wave speeds of the foam using travel time differences between sensor pairs. Our wave-speed estimates are 70 m/sec for *P* and 36 m/sec for *S*, with uncertainty estimates of about 2% and 4%, respectively. There is some suggestion of anisotropy of a few percent, which we neglect (but which is subsumed in the uncertainty estimates).

Nucleation

In order to simulate a unilaterally propagating strike-slip earthquake, events are artificially nucleated at one end of the fault plane by slightly raising one of the supporting jacks (jack D), bringing the fault at that end to near the point of shear failure. Several events were triggered spontaneously during the shear loading, without raising jack D. However, only the events that nucleated at one end of the fault (close to jacks C and D) were selected to study the effects of directivity.

Motion Sensors

Fault-normal and fault-parallel accelerometers are deployed on the free surface of the lower block along lines parallel to strike, to characterize the directivity-enhanced near-fault ground motion at distances of 25 and 45 cm away from the fault trace. Figure 3 shows the sensor locations with respect to the approximate hypocenter location and unstressed region. Coordinates of the sensors are given in Table 1. Each event was recorded with one of three different sensor configurations, which we refer to as configurations A, B, and C, respectively. All three configurations have the two along-strike profiles of fault-parallel and fault-normal sensors on the free surface. The configuration-A setup consists of two additional profiles of accelerometers positioned on the fault plane at depths of 10 and 40 cm. The configuration-B setup has a single profile of fault-plane accelerometers at a depth of 10 cm, and fault slip is measured

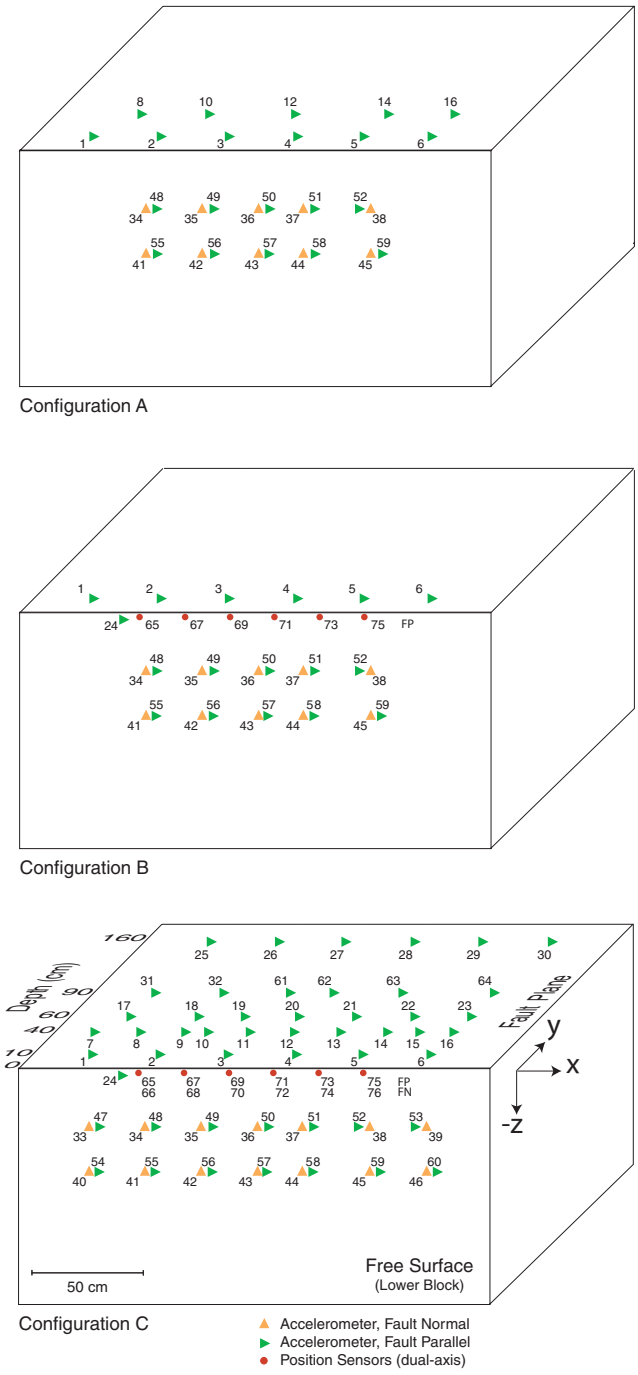

Figure 3. The three sensor configurations (A, B, and C) used for the experiments. Sensor coordinates are given in Table 1.

by a profile of displacement sensors located adjacent to the trace of the fault at the free surface. Configuration C has the displacement sensors on the fault trace, as well as five profiles of fault-plane accelerometers. About two-thirds of the experiments were done with the configuration-A setup and about one-third in the configuration-B setup. The extra sensors required for configuration C became available more recently, and only one of the experiments studied here was done with that sensor configuration.

Table 1
Location, Type, and Orientation of the Sensors in Figure 3

Sensor Number	Coordinates (x, y, z) (cm)	Sensor Type	Sensor Orientation	Sensor Number	Coordinates (x, y, z) (cm)	Sensor Type	Sensor Orientation
1	29, 10, −3	1	1	39	175, 3, −25	1	2
2	60, 10, −3	1	1	40	35, 3, −45	1	2
3	90, 10, −3	1	1	41	55, 3, −45	1	2
4	121, 10, −3	1	1	42	80, 3, −45	1	2
5	151, 10, −3	1	1	43	105, 3, −45	1	2
6	182, 10, −3	1	1	44	125, 3, −45	1	2
7	20, 41, −3	1	1	45	155, 3, −45	1	2
8	40, 41, −3	1	1	46	175, 3, −45	1	2
9	60, 41, −3	1	1	47	40, 3, −25	1	1
10	71, 41, −3	1	1	48	60, 3, −25	1	1
11	89, 41, −3	1	1	49	85, 3, −25	1	1
12	109, 41, −3	1	1	50	110, 3, −25	1	1
13	129, 41, −3	1	1	51	130, 3, −25	1	1
14	150, 41, −3	1	1	52	150, 3, −25	1	1
15	165, 41, −3	1	1	53	170, 3, −25	1	1
16	180, 41, −3	1	1	54	40, 3, −45	1	1
17	29, 60, −3	1	1	55	60, 3, −45	1	1
18	59, 60, −3	1	1	56	85, 3, −45	1	1
19	79, 60, −3	1	1	57	110, 3, −45	1	1
20	104, 60, −3	1	1	58	130, 3, −45	1	1
21	129, 60, −3	1	1	59	160, 3, −45	1	1
22	155, 60, −3	1	1	60	180, 3, −45	1	1
23	180, 60, −3	1	1	61	89, 90, −3	1	1
24	56, 3, −4	1	1	62	109, 90, −3	1	1
25	29, 160, −3	1	1	63	139, 90, −3	1	1
26	59, 160, −3	1	1	64	180, 90, −3	1	1
27	89, 160, −3	1	1	65	61, 0, −1	2	1
28	120, 160, −3	1	1	66	61, 0, −1	2	2
29	150, 160, −3	1	1	67	81, 0, −1	2	1
30	180, 160, −3	1	1	68	81, 0, −1	2	2
31	29, 90, −3	1	1	69	101, 0, −1	2	1
32	59, 90, −3	1	1	70	101, 0, −1	2	2
33	35, 3, −25	1	2	71	121, 0, −1	2	1
34	55, 3, −25	1	2	72	121, 0, −1	2	2
35	80, 3, −25	1	2	73	141, 0, −1	2	1
36	105, 3, −25	1	2	74	141, 0, −1	2	2
37	125, 3, −25	1	2	75	161, 0, −1	2	1
38	155, 3, −25	1	2	76	161, 0, −1	2	2

Sensor type: 1 (acceleration), 2 (displacement).
Sensor orientation: 1 (fault parallel), 2 (fault normal).

Numerical Model

Numerical simulations of the foam rubber earthquakes are performed using the 3D finite difference method developed by Day (1982a,b). That methodology has been reviewed in detail in recent papers (Day and Ely, 2002; Day *et al.*, 2005). It solves the linearized equations of motion for an isotropic elastic medium,

$$\boldsymbol{\sigma} = \rho(\alpha^2 - 2\beta^2)(\nabla \cdot \mathbf{u})\mathbf{I} + \rho\beta^2(\nabla\mathbf{u} + \mathbf{u}\nabla), \tag{1a}$$

$$\ddot{\mathbf{u}} = \rho^{-1}\nabla \cdot \boldsymbol{\sigma}, \tag{1b}$$

in which $\boldsymbol{\sigma}$ is the stress tensor, $\mathbf{u}$ is the displacement vector, α and β are the *P*- and *S*-wave speeds, respectively, ρ is density, and I is the identity tensor.

In the interior of each of two rectangular blocks, $\mathcal{D}^-$ and $\mathcal{D}^+$, the displacement field is twice differentiable and satisfies equation (1). These blocks are separated by a plane (the fault surface) Σ with unit normal $\hat{\mathbf{n}}$ directed from $\mathcal{D}^-$ to $\mathcal{D}^+$, across (at least part of) which they are in frictional contact. A discontinuity in the displacement vector is permitted across that interface, and the magnitude τ of shear traction vector $\boldsymbol{\tau}$, given by $(\mathbf{I} - \hat{\mathbf{n}}\,\hat{\mathbf{n}}) \cdot \boldsymbol{\sigma} \cdot \hat{\mathbf{n}}$, is bounded above by a nonnegative frictional strength τ_c. The limiting value of displacement as Σ is approached from the $\mathcal{D}^+$ ($\mathcal{D}^-$) side is denoted by $\mathbf{u}^+$ ($\mathbf{u}^-$). We write the discontinuity of the vector of tangential displacement as $\mathbf{s} \equiv (\mathbf{I} - \hat{\mathbf{n}}\,\hat{\mathbf{n}}) \cdot (\mathbf{u}^+ - \mathbf{u}^-)$, its time derivative by $\dot{\mathbf{s}}$, and their magnitudes by s and $\dot{s}$, respectively, and formulate the jump conditions at the interface as follows (Day *et al.*, 2005):

$$\tau_c - \tau \geq 0, \tag{2}$$

$$\tau_c\dot{\mathbf{s}} - \boldsymbol{\tau}\dot{s} = 0. \tag{3}$$

Equation (2) stipulates that the shear traction be bounded by friction, and equation (3) stipulates that any nonzero velocity discontinuity be opposed by an antiparallel traction ($\mathcal{D}^-$ exerts traction $-\boldsymbol{\tau}$ on $\mathcal{D}^+$) with magnitude equal to the frictional strength τ_c. The frictional strength evolves according to some constitutive functional that may in principle depend upon the history of the velocity discontinuity, and any number of other mechanical or thermal quantities, but is here simplified to the well-known slip-weakening form introduced by Ida (1972) and Palmer and Rice (1973). In that case, τ_c is the product of compressive normal stress $-\sigma_n$ and a coefficient of friction $\mu(\ell)$ that depends on the slip path length ℓ given by $\int_0^t \dot{s}(t')\,dt'$, and we use the linear slip-weakening form

$$\mu(\ell) = \begin{cases} \mu_s - (\mu_s - \mu_d)\ell/d_0 & \ell \le d_0, \\ \mu_d & \ell > d_0, \end{cases} \tag{4}$$

where μ_s and μ_d are coefficients of static and dynamic friction, respectively, and d_0 is the critical slip-weakening distance (e.g., Andrews, 1976; Day, 1982b, Madariaga *et al.*, 1998).

The blocks may also undergo separation over portions of the contact plane if there is a transient reduction of the compressive normal stress to zero (Day, 1991). We denote the normal component of traction on Σ (tension positive) by σ_n and the normal component of the displacement discontinuity by U_n, with jump conditions (Day *et al.*, 2005)

$$\sigma_n \le 0, \tag{5}$$

$$U_n \ge 0, \tag{6}$$

$$\sigma_n U_n = 0, \tag{7}$$

corresponding, respectively, to nontensile normal stress, no interpenetration, and loss of contact only if accompanied by zero normal stress. Loss of contact does not actually occur in any of the simulations performed for the current study. In fact, due to the symmetries of the problem and the assumption that the fault is planar, σ_n remains constant during the fault motion in our theoretical model. Roughness of the fault in the actual foam model undoubtedly results in small-scale fluctuations of the normal stress about its initial value during each experimental earthquake, with concomitant fluctuations in shear resistance. It is even possible that the aggregate effect of those fluctuations controls, in whole or in part, the macroscopic frictional behavior of the foam. Our theoretical model simply absorbs any such microscale effects on shear resistance into the macroscopic friction law (4). As shown in subsequent sections (and by Day and Ely, 2002), the resulting numerical model still mimics the smooth part of the foam-model accelerations very well, apparently justifying this procedure.

Our theoretical model for the foam rubber experiment approximates the bottom and top (i.e., the faces attached to the floor and the loading cell, respectively) of the apparatus as fixed boundaries, which is a fairly good approximation to their actual behavior (very good in the case of the bottom). The front face (corresponding to the Earth's free surface) and back face are treated as a free boundaries, which corresponds well to the experimental setup. In the experimental setup, portions of the end faces are attached to plywood sheets. We approximate those portions of the end faces as fixed boundaries, and the remainder of those faces as free boundaries. Because the plywood sheets on the ends of the upper block are hinged to the top, and the sheets on the ends of the lower block are hinged to the bottom, the fixed-boundary assumption is of limited validity in the case of the ends. A better approximation would be to treat them as single degree-of-freedom, rigid masses. However, our focus is principally on the initial acceleration pulses in the foam model. These are affected only by the end boundary nearest the hypocenter, because reflections from other boundaries occur late in time and are well separated from the initial acceleration pulse (and will be windowed out in our analysis). The effect of the near-end boundary is not negligible in its effect on the late-time displacement, because the fixed-boundary approximation results in events with final displacements that taper to zero at the fault ends, unlike the actual experimental events. However, the rigidity and inertia of the plywood sheets means that the fixed approximation is fairly good for times short compared with the transit time of the *S* wave across a sheet (of order 0.02 sec); this makes fixed boundaries a better approximation than free boundaries insofar as effects on the initial acceleration pulses are concerned.

The shear prestress vector on Σ is approximated as a constant, $\tau_0\hat{\mathbf{m}}$ (τ_0 nonnegative and $\hat{\mathbf{m}}$ the unit vector giving the prestress direction, which in this study is aligned with the fault strike direction), over the upper half of the fault surface (as described in the last section), which extends to depth W and has along-strike length L. The shear prestress in the lower portion of the model is also assumed constant but with a smaller absolute value as described previously. The negative of the normal stress, $-\sigma_n$, is assumed constant and denoted by σ_0. An event is nucleated artificially by reducing the coefficient of friction to μ_d over a circular area centered at a fixed hypocentral point (specified by a pair of fault-plane coordinates ξ_1, ξ_2) near one end of the fault, growing at speed $\beta/2$.

Dimensional Analysis

The theoretical model described previously determines a displacement field that is a function of three spatial coordinates, time, and 10 parameters: α, β, ρ, τ_0, σ_0, μ_s, μ_d, d_0, W, and L. We do not consider variations in hypocenter (ξ_1, ξ_2) and ignore length scales associated with the finite size of the blocks.

If we define $\Delta\tau$ and $\tilde{S}$ by

$$\Delta\tau \equiv \tau_0 - \sigma_0\mu_d, \tag{8}$$

$$\tilde{S} \equiv \frac{\sigma_0(\mu_s - \mu_d)}{\Delta\tau} \tag{9}$$

(noting that $\tilde{S} = S + 1$, where S is Andrews' (1976) often-cited ratio of stress excess to stress drop), then taking advantage of the fact that there is no fluctuation of normal stress in this model, we can write the friction law (4) as

$$\tau_c = \tau_0 + \Delta\tau[\tilde{S}\psi(\ell/d_0) - 1] \tag{10}$$

with $\psi(z) = (1 - z)H(z)H(1 - z)$, where H is the Heaviside step function (though the analysis would apply unchanged to any form of the function ψ, subject to $\tau_c \geq 0$). The initial normal stress σ_0 thus enters only through $\tilde{S}$ and $\Delta\tau$, and we can reduce the four parameters τ_0, σ_0, μ_s, and μ_d to the new set of three, τ_0, $\Delta\tau$, and $\tilde{S}$.

We initially choose the following set of independent dimensionless quantities (distinguished by tildas):

$$\tilde{x}_i \equiv x_i/W, \qquad i = 1, 2, 3; \qquad \tilde{t} \equiv \beta t/W; \qquad \tilde{A} \equiv \alpha/\beta;$$
$$\tilde{L} \equiv L/W; \qquad \tilde{S} \equiv \frac{\sigma_0(\mu_s - \mu_d)}{\Delta\tau}; \qquad \tilde{D} \equiv \frac{\rho\beta^2 d_0}{\Delta\tau W};$$
$$\tilde{F} \equiv \Delta\tau/\tau_0; \qquad \tilde{\Delta} \equiv \Delta\tau/\rho\beta^2$$

in terms of which the displacement can be written as

$$u_i = W\varphi_i(\tilde{\mathbf{x}}, \tilde{t}; \tilde{A}, \tilde{L}, \tilde{S}, \tilde{D}, \tilde{F}, \tilde{\Delta}), \tag{11}$$

where the vector $\boldsymbol{\phi}$ satisfies

$$\ddot{\phi}_i = \Sigma_{ij,j}, \tag{12}$$

where

$$\Sigma_{ij} = (\tilde{A}^2 - 2)\phi_{k,k}\delta_{ij} + \phi_{i,j} + \varphi_{j,i} \tag{13}$$

(in which spatial and temporal derivatives are taken with respect to dimensionless coordinates). Taking $\hat{\mathbf{e}}_1 = \hat{\mathbf{m}}$ and $\hat{\mathbf{e}}_3 = \hat{\mathbf{n}}$ and noting that (because $\dot{\phi}_1^+ = -\dot{\phi}_1^-$ and $\dot{\phi}_2^+ = -\dot{\phi}_2^-$ under the assumptions made) $\dot{\mathbf{s}} = 2\beta(\dot{\phi}_1^+\hat{\mathbf{e}}_1 + \dot{\phi}_2^+\hat{\mathbf{e}}_2)$, the conditions (2) and (3) take the form

$$1 + \tilde{F}\left[\tilde{S}\psi\left(\frac{\ell}{W\tilde{\Delta}\tilde{D}}\right) - 1\right] - [(1 + \tilde{F}\tilde{\Delta}^{-1}\Sigma_{31})^2 + (\tilde{F}\tilde{\Delta}^{-1}\Sigma_{32})^2]^{1/2} \geq 0 \tag{14}$$

and

$$\left\{1 + \tilde{F}\left[\tilde{S}\psi\left(\frac{\ell}{W\tilde{\Delta}\tilde{D}}\right) - 1\right]\right\}(\hat{\mathbf{e}}_1\dot{\phi}_1^+ + \hat{\mathbf{e}}_2\dot{\phi}_2^+) - [\hat{\mathbf{e}}_1 + \tilde{F}\tilde{\Delta}^{-1}(\hat{\mathbf{e}}_1\Sigma_{31}^+ + \hat{\mathbf{e}}_2\Sigma_{32}^+)][(\dot{\phi}_1^+)^2 + (\dot{\phi}_2^+)^2]^{1/2} = 0. \tag{15}$$

We can simplify considerably by assuming that $\tilde{F}$ is sufficiently small such that $\tilde{F}\tilde{\Delta}^{-1}\Sigma_{31}$ does not fall below -1 (i.e., the initial shear stress is sufficiently large compared with the stress drop that dynamic stress overshoots can never reverse the sense of slip) and such that $|\tilde{F}\tilde{\Delta}^{-1}\Sigma_{32}|$ is small compared with 1. Dunham (2005) has shown that slip transverse to the prestress direction is suppressed by an effective viscosity proportional to $\tilde{F}^{-1}$, so that in the limit of small $\tilde{F}$, slip becomes constrained to the prestress direction. Experience with numerical solutions shows that this constraint on slip direction holds reasonably well for any $\tilde{F}$ meeting the aforementioned no-reversal criterion, and we make that approximation here. With these approximations, (14) and (15) reduce to

$$\tilde{S}\psi\left(\frac{2\phi_1^+}{\tilde{\Delta}\tilde{D}}\right) - 1 - \tilde{\Delta}^{-1}\Sigma_{31} \geq 0, \tag{16}$$

$$\left[\tilde{S}\psi\left(\frac{2\phi_1^+}{\tilde{\Delta}\tilde{D}}\right) - 1\right]\dot{\phi}_1^+ - \tilde{\Delta}^{-1}\Sigma_{31}^+|\dot{\phi}_1^+| = 0, \tag{17}$$

so to this level of approximation, the dependence on $\tilde{F}$ drops out.

We note that if $\boldsymbol{\phi}^{(1)}$ is the solution to (12) to (15) for $\tilde{\Delta} = \tilde{\Delta}_1$, then $(\tilde{\Delta}_2/\tilde{\Delta}_1)\boldsymbol{\phi}^{(1)}$ is the solution for $\tilde{\Delta} = \tilde{\Delta}_2$, and therefore we can write the equations in the reduced form

$$u_i = \frac{W\Delta\tau}{\rho\beta^2}\boldsymbol{\Phi}_i(\tilde{\mathbf{x}}, \tilde{t}; \tilde{A}, \tilde{L}, \tilde{S}, \tilde{D}), \tag{18}$$

$$\ddot{\boldsymbol{\Phi}}_i = [(\tilde{A}^2 - 2)\boldsymbol{\Phi}_{k,k}\delta_{ij} + \boldsymbol{\Phi}_{i,j} + \boldsymbol{\Phi}_{j,i}]_{,j}, \tag{19}$$

$$\tilde{S}\psi\left(\frac{2\boldsymbol{\Phi}_1^+}{\tilde{D}}\right) - 1 - (\boldsymbol{\Phi}_{1,3}^+ + \boldsymbol{\Phi}_{3,1}^+) \geq 0, \tag{20}$$

$$\left[\tilde{S}\psi\left(\frac{2\boldsymbol{\Phi}_1^+}{\tilde{D}}\right) - 1\right]\dot{\boldsymbol{\Phi}}_1^+ - (\boldsymbol{\Phi}_{1,3}^+ + \boldsymbol{\Phi}_{3,1}^+)|\dot{\boldsymbol{\Phi}}_1^+| = 0, \tag{21}$$

where $\boldsymbol{\Phi} \equiv \partial\boldsymbol{\phi}/\partial\tilde{\Delta}$ is now independent of $\tilde{\Delta}$. That is, the solution is characterized by four dimensionless parameters: $\tilde{A}$ (wave-speed ratio α/β), $\tilde{L}$ (fault aspect ratio L/W), $\tilde{S}$ (one plus dimensionless stress excess), and $\tilde{D}$ (dimensionless weakening displacement $\rho\beta^2 d_0/\Delta\tau W$).

The mean final slip $\bar{s}$ scales with $\Delta\tau W/\rho\beta^2$, with a geometry-dependent constant of proportionality of order 1. In the geometry of our numerical model for the foam events, the approximation $\bar{s} \approx \Delta\tau W/\rho\beta^2$ is accurate to within 20% or so, and with this approximation, $\tilde{D} \approx d_0/\bar{s}$, i.e., $\tilde{D}$ can be interpreted as the ratio of the weakening slip to mean final slip. Another dimensionless ratio of interest that can be derived from the others is $\tilde{D}\,\tilde{S}/2$. This number is proportional to the ratio $G/(\Delta\tau\bar{s})$, where G is the fracture energy and $\bar{s}$ is the mean final slip, and with the same approximation as before we have $\tilde{D}\,\tilde{S}/2 \approx G/(\Delta\tau\bar{s})$.

Experimental Events

A total of 43 foam rubber earthquakes make up the data set. Most of these experiments (72%) were done with $-\sigma_n$ set to 320 Pa, while a smaller percentage of events have $-\sigma_n$ set to 385 Pa (21%) or 538 Pa (7%). All events are similar in that they nucleated near one end of the fault (the same end in all cases) and the rupture propagated predominantly unilaterally.

A principal objective is to understand rupture-directivity-induced effects on ground motion. It is therefore important to investigate rupture propagation direction, speed, and variability in the foam rubber experiments. For each event recorded in configuration A (see Fig. 3), we picked first arrival times for each sensor from the two profiles of fault-parallel accelerometers located on the fault plane. Each arrival time was plotted on the fault plane at the corresponding sensor location. We then constructed rupture-front contours from these arrival times. We have rupture-time contours for a total of 29 events (it was not possible to do this for configuration B events because there is only one along-strike profile of fault-plane accelerometers).

Comparison of the rupture-front contours reveals considerable variability in hypocenter depth among individual events. Two end member types of events are identified on the basis of rupture geometry: events that are horizontally rupturing (type I) and events that are strongly obliquely rupturing, indicating a very deep hypocenter (type II). Rupture contours illustrating an event typical of each type are shown in Figure 4 (Gonzalez [2003] presents the rupture contours for all configuration A events used in the analysis). We classified as type II those events having one or more contours indicating predominantly up-dip rupture propagation, defined as incidence angle less than 35° (i.e., wavefront normal less than 35° to the vertical). On this basis, most (24) of the 29 events for which we have rupture contours are of the predominantly horizontally rupturing type-I class.

Acceleration time series representative of the two main types of events also exhibit differences due to the different

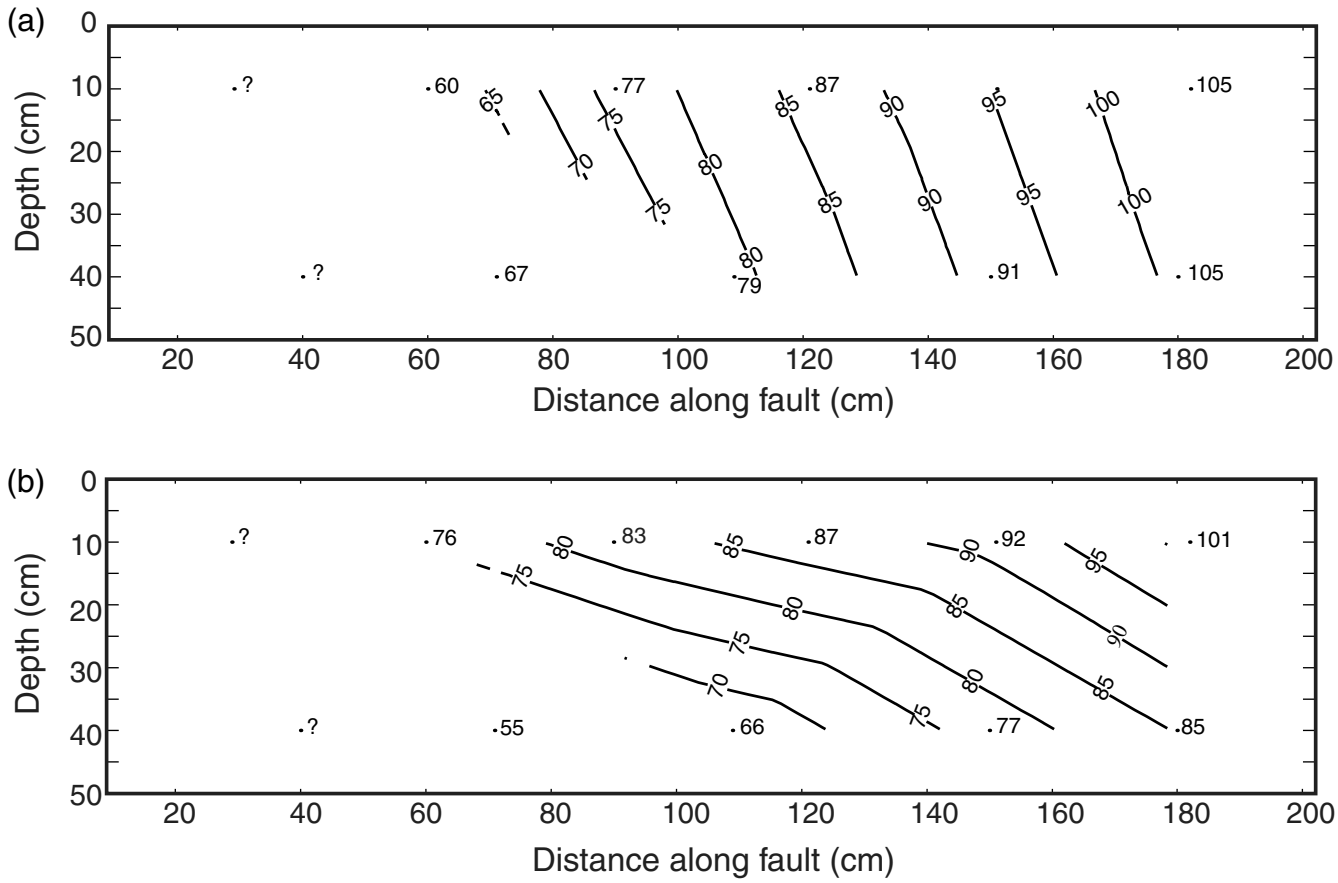

Figure 4. Rupture contours for typical foam-model events of (a) type I (horizontally rupturing) and (b) type II (obliquely rupturing).

rupture geometries. Figure 5 shows acceleration time series for the two ruptures contoured in Figure 4, for selected sensors 25 cm from the fault trace. Events in which the rupture is predominantly horizontal, or type-I events, exhibit the largest maximum accelerations on the fault-normal component at the largest distances along the strike of the fault. Fault-parallel components also increase in amplitude as distance along strike increases, but at a lower rate of increase than the fault-normal components, and are therefore lower than the fault-normal component except at the sensor closest to the hypocenter. Events in which rupture is predominantly upward, or type-II events, exhibit the largest fault-parallel accelerations at intermediate distances along strike. The fault-normal component is largest at the end of the fault as for type-I events. However, the main acceleration pulse consists of a double peaked pulse, rather than a large single peaked pulse. Using these accelerogram characteristics, we classified as type I or type II those remaining events for which we do not have rupture contours (i.e., those recorded with sensor configuration B). In total, 35 of the original 43 events are of type I. In order to focus on ground-motion effects induced by along-strike rupture propagation, all further analysis in this article will be restricted to the type-I events.

We estimated rupture velocities for the 24 type-I events with rupture contours, and the results are given in Table 2. Velocity of the rupture-front for each event was calculated by measuring the perpendicular distance between two adjacent contours. This distance was then divided by the time interval between the two respective contours to estimate the velocity of rupture. It was possible to obtain rupture-velocity estimates for along-strike propagation distances ranging from 100 to 180 cm, and the mean rupture velocity taken over all (type-I) events is plotted as a function of along-strike distance in Figure 6. Rupture accelerates between 100 and 140 cm distance, beyond which it is nearly independent of distance, with a mean value of 32.5 m/sec (and standard deviation of ± 2.0 m/sec). This apparently limiting rupture velocity is equal to 0.9 times the S velocity, and within experimental error, this is not distinguishable from the Rayleigh-wave velocity of the foam (0.93 times the S velocity, based on the measured P- to S-velocity ratio). A terminal velocity near the Rayleigh velocity is consistent with predictions of dynamic fracture mechanics for the case of mode II crack extension.

Numerical Modeling Results

Before proceeding to an analysis of directivity, we model one of the experimental events numerically and compare the synthetic and recorded waveforms. Table 3 gives the values of the numerical-model parameters used to simulate one of the experimental events for which initial normal stress was 538 Pa (simulation 1). This was the only experiment in the study done with the more extensively instrumented configuration C. The hypocenter of the experimental event is near an end of the fault but is otherwise not known with precision; we nucleate the numerical simulation 30 cm from the end, and at middepth (50 cm) on the fault. The numerical model used an initial shear-stress value of 651 Pa, about one standard deviation below the experimental mean noted earlier (from Fig. 2). We used the dynamic friction coefficient $\mu_d = 1.09$ inferred from Figure 2. Following the discussion in Day and Ely (2002), we assumed that the weakening displacement (d_0) is comparable to the typical ~1 mm dimension of the foam rubber vesicles. Its value,

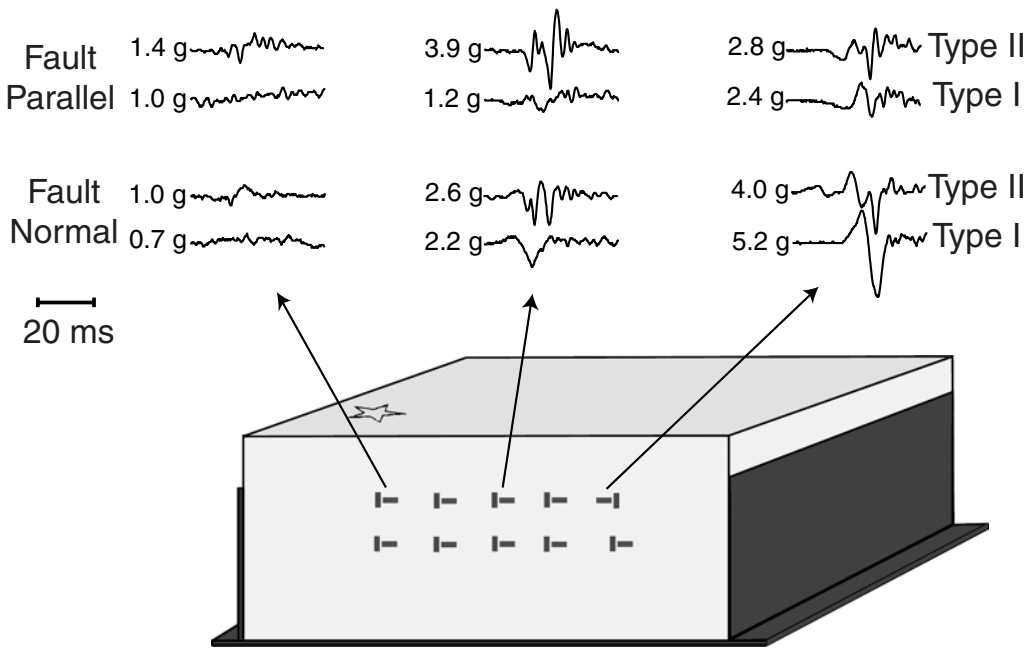

Figure 5. Acceleration time series for the two ruptures contoured in Figure 4, for selected sensors 25 cm from the fault trace.

Table 2

Rupture-Velocity Estimates, as a Function of Epicentral Distance

	Distance (cm)								
Event ID	100	110	120	130	140	150	160	170	180
jn03		23.1	33.0	31.9	31.9	31.9	33.0	33.0	
jn04		28.6	30.6	30.8	30.8	30.8	31.9	31.9	
jn05		26.4	26.4	26.8	26.8	26.8	26.8	28.6	
jn06		26.8	29.7	30.4	30.8	30.8	30.8	34.1	34.1
jn08		24.2	30.8	28.8	28.8	29.0	31.2	31.2	
jn09		30.4	30.4	33.0	34.8	34.8	34.8	34.8	
jn11		30.8	34.3	34.3	34.1	33.4	33.4	30.8	
jn13		33.0	33.0	29.7	32.8	32.8	33.0	33.0	
jn18		27.5	27.5	31.0	31.0	31.0	30.2	30.2	30.2
jn20		28.1	28.1	33.0	33.0	33.0	31.4	31.4	31.4
jn23		31.9	26.6	26.6	34.1	34.1	34.1		
jn27				33.0	33.0	33.0	37.0	37.0	
jn31		32.6	32.6	35.2	35.2	35.2	35.2	35.2	
SG01	25.3	33.0	33.0	33.4	34.1	34.1			
SG03		27.5	28.1	28.1	31.0	31.2	31.2		
SG04		30.8	30.8	34.1	34.8	34.8			
SG05	24.2	28.6	31.9	31.9	31.9	31.9	31.9		
SG06		29.0	29.0	30.8	32.6	32.6	31.7		
SG07		24.2	28.6	31.9	31.9	31.9			
SG08		30.8	31.9	33.0	33.0	33.7	33.7		
SG09		33.4	31.9	31.9	31.9	31.9	32.1		
SG10		33.4	33.4	33.4	34.1	34.1			
SG11		34.8	32.1	32.1	33.0	33.0	32.6		
SG12	26.4	33.0	33.0	33.0	33.0	33.0			
Mean	25.3	29.7	30.7	31.6	32.4	32.5	32.4	32.6	31.9
Standard deviation	1.1	3.3	2.3	2.3	2.0	1.9	2.2	2.4	2.0

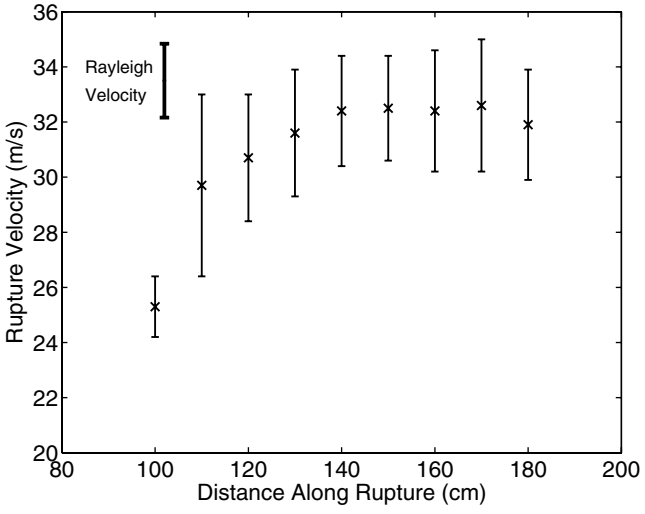

Figure 6. Rupture velocity as a function of along-strike propagation distance. The figure shows means and standard deviations for experimental events of type I (predominantly along-strike rupture direction).

as well as the static coefficient of friction μ_s, were adjusted to obtain a good fit to the rupture velocity, as reflected in the arrival time moveout of the fault-parallel slip-velocity pulse recorded at 10-cm depth on the fault plane. This criterion was met by values of $d_0 = 0.6$ mm and $\mu_s = 1.35$.

Slip Velocities

Figure 7 shows the experimental and synthetic velocity (from numerical integration of the fault-parallel acceleration) on the fault. From the symmetry of the experiment, this equals approximately (exactly, in the case of the numerical simulation) 0.5 times the slip-velocity time history. The experimental-event origin time is not known, so the time scale for all the experimental data (both fault plane and free surface) has been given a common time shift (i.e., preserving all relative times) to align the experimental- and numerical-simulation pulses on sensor 5 (at 10-cm depth on the fault plane). Significant boundary reflections from the far end of the foam block arrive after about 0.22 sec, and the plots have been truncated before those arrivals occur. An irregular, short-period (a few milliseconds or less) component is present in the experimental data that is not modeled (and would

Table 3
Numerical-Model Parameters

Model Parameter	Simulation 1	Simulation 2	Simulation 3
Initial shear stress (Pa) (τ_0)	651	438	438
Initial normal stress (Pa) ($-\sigma_n$)	538	320	320
Static friction coefficient (μ_s)	1.35	1.54	1.49
Dynamic friction coefficient (μ_d)	1.09	1.22	1.22
Critical slip distance (mm) (d_0)	0.6	0.35	0.35

be beyond the resolution of the numerical simulations). We will confine attention to the longer-period component of the records.

The numerical simulation reproduces the shape, duration, and amplitude of the experimental slip-velocity pulse, as well as its propagation velocity, with remarkable fidelity, at all 16 sensors at 10- and 40-cm depth. At 60-cm depth, the waveforms are still well modeled, but with some delay of the numerical-model arrivals. The rupture delay of the numerical model is even more pronounced at 90-cm depth. This delay may be a result of the assumption of uniform initial shear stress in the numerical model. The experimental loading procedure described earlier would be expected to concentrate stress near the bottom edge of the fault when the load on the lower half transfers to the upper half, and the higher initial stress should accelerate rupture. We did not attempt to account for this effect in the numerical model. The records at 160-cm depth show no motion, confirming that the lower part of the fault was successfully locked by the loading procedure (although uncertainty remains about the locking depth).

Surface Accelerations

Figure 8 shows fault-normal- and fault-parallel-component accelerations for the along-strike free-surface sensor profiles. As with the fault slip, some very short-period, incoherent motion is present in the experimental records. This high-frequency component is proportionally much lower at the free-surface sensors than it is on the fault plane (although this is not obvious from a comparison of Figs. 7 and 8, because the former shows velocity and the latter acceleration). The numerical simulation captures the coherent, longer-period acceleration pulses, in shape, duration and amplitude, and timing, on all 28 free-surface accelerometers. In particular, the systematic increase in fault-normal acceleration amplitude with propagation distance is well reproduced. The rapid decrease in amplitude from 25- to 45-cm distance from the fault is also very well modeled, as are the relative amplitudes of fault-normal and fault-parallel motion. Figure 8 also shows the fault-plane displacements (half the slip), which are underpredicted by about a factor of 2. The underprediction is partly a consequence of the rigid boundary condition used in the numerical simulations at the ends of the fault; a second factor may be penetration of slip to a greater depth in the experiments than the 1 m assumed in the simulation.

The similarity of recorded and synthetic accelerations and slip velocities indicates that the experimental events can be understood, at least macroscopically, as relatively simple, propagating shear failures with approximately uniform stress drops. There are unmodeled short-period (of the order of milliseconds) oscillations in the records that indicate more complex behavior at the centimeter scale, probably including normal-stress fluctuations, and possibly even

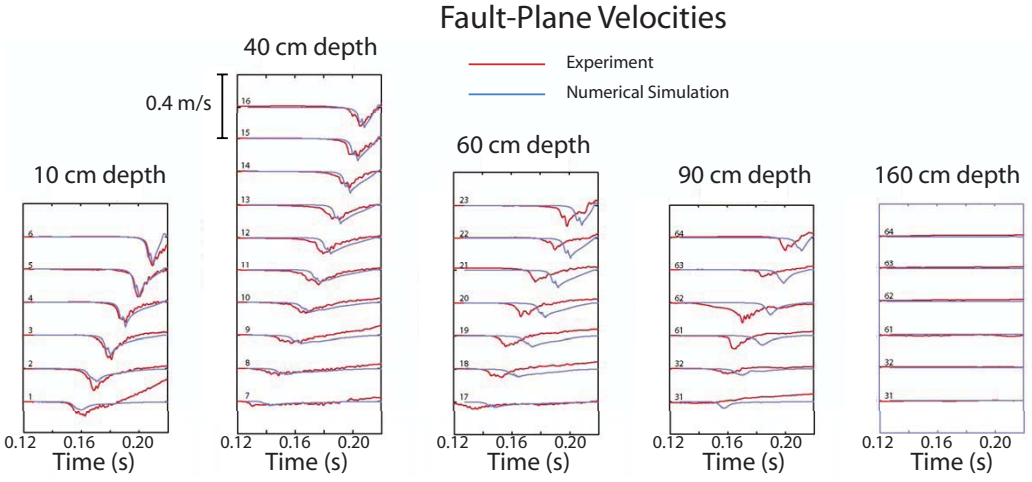

Figure 7. Velocity on the fault for experiment (at 538 Pa normal stress) and simulation 1. Velocity represents one-half the fault slip rate.

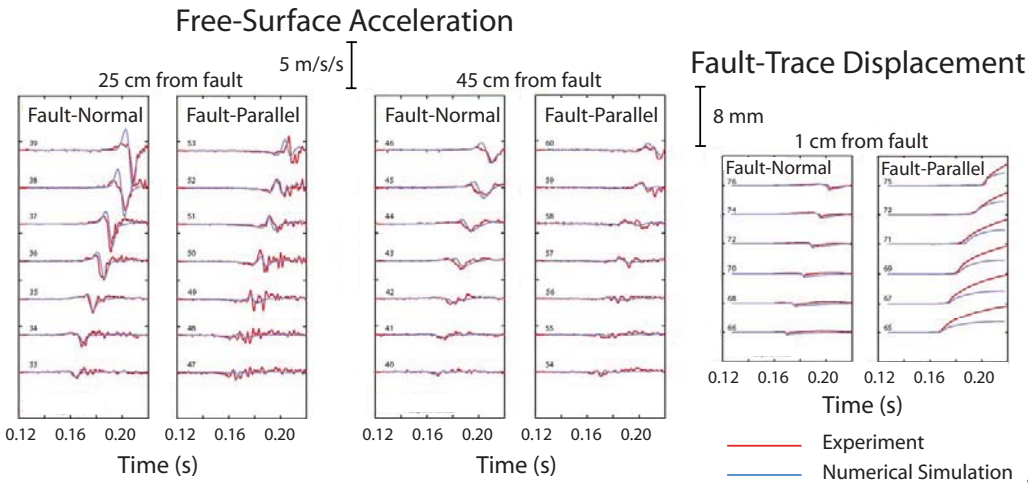

Figure 8. Free-surface accelerations and fault-trace displacements for same experiment shown in Figure 7.

small-scale fault opening. However, the agreement between experimental and numerical simulation is evidence that, if such processes are present, they are not coherent at larger scales, where they can be successfully represented by a simple frictional sliding model. The mode of slip is clearly cracklike rather than pulselike, as also concluded by Day and Ely (2002) from analysis of less extensively instrumented foam rubber experiments. The comparison also confirms the adequacy of elastodynamics as a model for the foam rubber medium and suggests that the experimental data are free of significant artifacts associated with loading apparatus, sensor inertia or coupling, or boundaries (prior to about 0.22 sec), except for the effect on displacements noted before. On the other hand, the quality of agreement between recorded and synthetic accelerations should not be taken as substantiation for the precise parameter values used in the numerical simulation. First of all, some trade-offs are possible among the values of τ_0, d_0, and the friction coefficients. That is, the experimental acceleration records can be fit about as well by other combinations of these parameters that are still consistent with experimental bounds on their values (e.g., Gonzalez, 2003). Furthermore, there is some experimental variability among events; peak acceleration for experiments at a given normal stress (and given distance) has a standard deviation approximately 40% of the mean.

Dimensionless Ratios

We can use the measured parameter values for the foam rubber, together with the additional parameter values suggested by simulation 1 (Table 3), to make estimates of the four dimensionless parameters appropriate to the model. Then, to the extent possible, we can assess their relationship to the comparable dimensionless ratios for large natural earthquakes. In the foam rubber experiments, the wave-speed ratio A is approximately 1.9, not too different from the values of ~1.7–1.8 typical of crystalline crustal rocks. $\tilde{L}$ in the experiments is approximately 2, which, assuming a seismogenic depth of ~12 km, would correspond to an earthquake of moment magnitude of roughly 6.7.

Assessment of dimensionless ratios $\tilde{D}$ and $\tilde{S}$ is less straightforward. We will use parameter values (d_0, μ_s, μ_d, σ_0, and τ_0) from simulation 1, Table 3, but note again that d_0 and μ_s were determined indirectly by examining waveform agreements between experiments and numerical simulations. These parameters result in $\tilde{D} \sim 0.2$. As noted previously, mean final slip $\bar{s}$ is approximately $\Delta\tau W/\mu$, and we can interpret $\tilde{D}$ as the ratio of d_0 to mean final slip. While this ratio implies weakening displacements orders of magnitude larger than required to explain the nucleation behavior of natural earthquakes, it is of the same order of magnitude as d_0 values inferred from seismic observations (e.g., Ide and Takeo, 1997; Bouchon *et al.*, 1998; Mikumo *et al.*, 2003) and is roughly consistent with the weakening displacements observed in some laboratory rock experiments at high slip velocity (Goldsby and Tullis, 2002; DiToro *et al.*, 2004). The value of $\tilde{S}$ for the experiments is ~2.2, corresponding to an S ratio (strength excess to stress drop) of 1.2. For natural earthquakes, Abercrombie and Rice (2005) estimate a lower bound on S of ~0.8 from analysis of earthquake spectral parameters. They argue, however, that considerably higher values are likely, because the seismic estimates are insensitive to significant friction reduction occurring in the first fraction of a millimeter of slip.

With the estimates of both S and d_0 being quite uncertain, a better comparison might be one expressed in terms of fracture energy (e.g., Guatteri and Spudich, 2000; Tinti *et al.*, 2005). Abercrombie and Rice (2005) estimate the dimensionless ratio $G/(\Delta\tau\bar{s})$, which, as we have noted, is approximately equal to $\tilde{D}\,\tilde{S}/2$ in our model. Under the assumption that static stress is equal to final frictional stress (no overshoot or undershoot), Abercrombie and Rice find $G/(\Delta\tau\bar{s}) \approx 0.25$. For our model $\tilde{D}\,\tilde{S}/2$ is 0.22.

Free-Surface Breakout and Supershear Transition

We have not seen any unambiguous evidence of supershear rupture velocity in any of the experimental events for which rupture contours can be constructed. However, it is relatively easy, beginning with a numerical model for which rupture velocity is everywhere sub-Rayleigh, and that fits the experimental waveform data well, to induce a supershear transition by introducing relatively small model perturbations. Even introducing a small amount of bilaterality to the rupture by moving the nucleation point well away from the end of the fault (holding all other parameters fixed) in some cases leads to a supershear transition that is otherwise absent (Gonzalez, 2003). Because we have not observed the transition in the laboratory experiments, it seems likely that the actual μ_s in the experimental model is substantially higher than we have assumed, because a higher value would inhibit the transition. In that case, our numerical explorations have probably only constrained the fracture energy (or, in dimensionless terms, only constrained the product $\tilde{D}\,\tilde{S}$—the ratio of fracture energy to seismic energy—rather than the two factors separately).

In any case, the supershear transition mechanism in the numerical simulations themselves merits some discussion. We will base the discussion on Figure 9, showing a sequence of images of fault-parallel slip velocity in the fault plane for two simulations, simulations 2 and 3. The model parameters are given in Table 3 and differ only in the value of μ_s. Simulation 2 (Fig. 9a), which matched experimental waveforms for the 320 Pa normal-stress events quite well, has sub-Rayleigh rupture velocity throughout. In simulation 3 (Fig. 9b), a supershear transition occurs, beginning between the 39- and 45-msec frames. The supershear rupture front seems to emerge smoothly from the free-surface intersection point of the main sub-Rayleigh front, rather than initiating as a daughter crack ahead of the main front, as predicted for homogenous faults in the absence of a free surface (Andrews, 1976; Dunham, 2007). Careful analysis of higher-resolution calculations would be required before we could rule out a very small-scale daughter-crack mechanism, however.

In numerous other cases with this geometry that we have examined, the nucleation of the supershear transition invariably occurred at the intersection of the rupture with the free surface. This tendency for numerically simulated ruptures to accelerate to supershear velocity at the free surface has been noted previously (e.g., Olsen *et al.*, 1997; Aagaard *et al.*, 2001; Gonzalez, 2003). We make two observations: (1) At least in the case studied here, the transition would not have occurred at all in the absence of the free-surface interaction, as we can see by an application of Dunham's (2007) analysis of intersonic crack nucleation ahead of self-similar cracks with slip-weakening friction. The value of the normalized strength excess S for simulation 3 is ~0.8. Dunham's analysis would predict the transition under homogenous conditions (with no free surface) to occur only after propagation over a distance L_{trans}, which in this case is more than twice the maximum model dimension L (this estimate is arrived at using Fig. 5 of Dunham [2007], also taking into account the observation therein that L_{trans} is reduced by another factor of ~3 for the case of linear slip weakening, compared with the weakening model used to construct that figure). (2) The surface breakout of rupture provides a natural mechanism for accelerating rupture by generating a secondary, reflected slip pulse in the fault plane. This secondary pulse is visible in both simulations shown in Figure 9. Along the free surface the secondary pulse is coincident with the main rupture front, providing an additional stress transient to accelerate the rupture front into the intersonic regime, in a manner analogous to rupture acceleration by similar transients (induced by, e.g., stress-drop and fracture energy perturbations) that have been analyzed in detail by Dunham *et al.* (2003) and Dunham (2007). From an analysis of similar simulations with surface breakout, Kaneko *et al.* (2007) provide a more detailed explanation, identifying the free-surface S to P conversion as the principal pulse driving the transition. Also note that the rupture front becomes distorted into a concave shape at and just below the free surface, and the resulting focusing might further contribute to localizing the transition in that area.

It is questionable how efficiently this free-surface effect would act to accelerate rupture on natural faults. Day and Ely (2002) identified and modeled breakout-induced secondary slip pulses in the scale-model earthquake experiments of Brune and Anooshehpoor (1998). However, the secondary pulses are rapidly attenuated when stress release on the upper portion of the fault is suppressed, either by introducing velocity-strengthening friction (Brune and Anooshsehpoor, 1998) or a very low slip-weakening slope (Day and Ely, 2002). Nonetheless, there is now considerable seismic evidence for supershear episodes in large, surface-rupturing earthquakes (e.g., Archuleta, 1984; Bouchon *et al.*, 2001; Bouchon and Vallee, 2003; Dunham and Archuleta, 2004), and the role of surface breakout as a mechanism for the supershear transition deserves a more complete analysis than we have available at present.

Response Spectra

We calculated response spectra (pseudospectral acceleration, 5% damping) for a subset of the foam experiments consisting of all type-I events with normal stress $\sigma_n = 320$ Pa. This subset comprises a majority of the type-I events, and provides a homogeneous data set from which to obtain averages. The records were windowed to exclude all large boundary reflections. Figure 10 shows mean spectral accelerations for this set of foam events. Also shown are corresponding spectra for a numerical simulation of a $\sigma_n = 320$ Pa event. Table 3 gives the model parameters for this calculation, which is denoted simulation 2. Spectra are shown for sensors located 25 and 45 cm from the fault trace, at both the shortest ($x = 55$ cm) and longest ($x = 155$ cm) along-strike distances. The mean fault-parallel

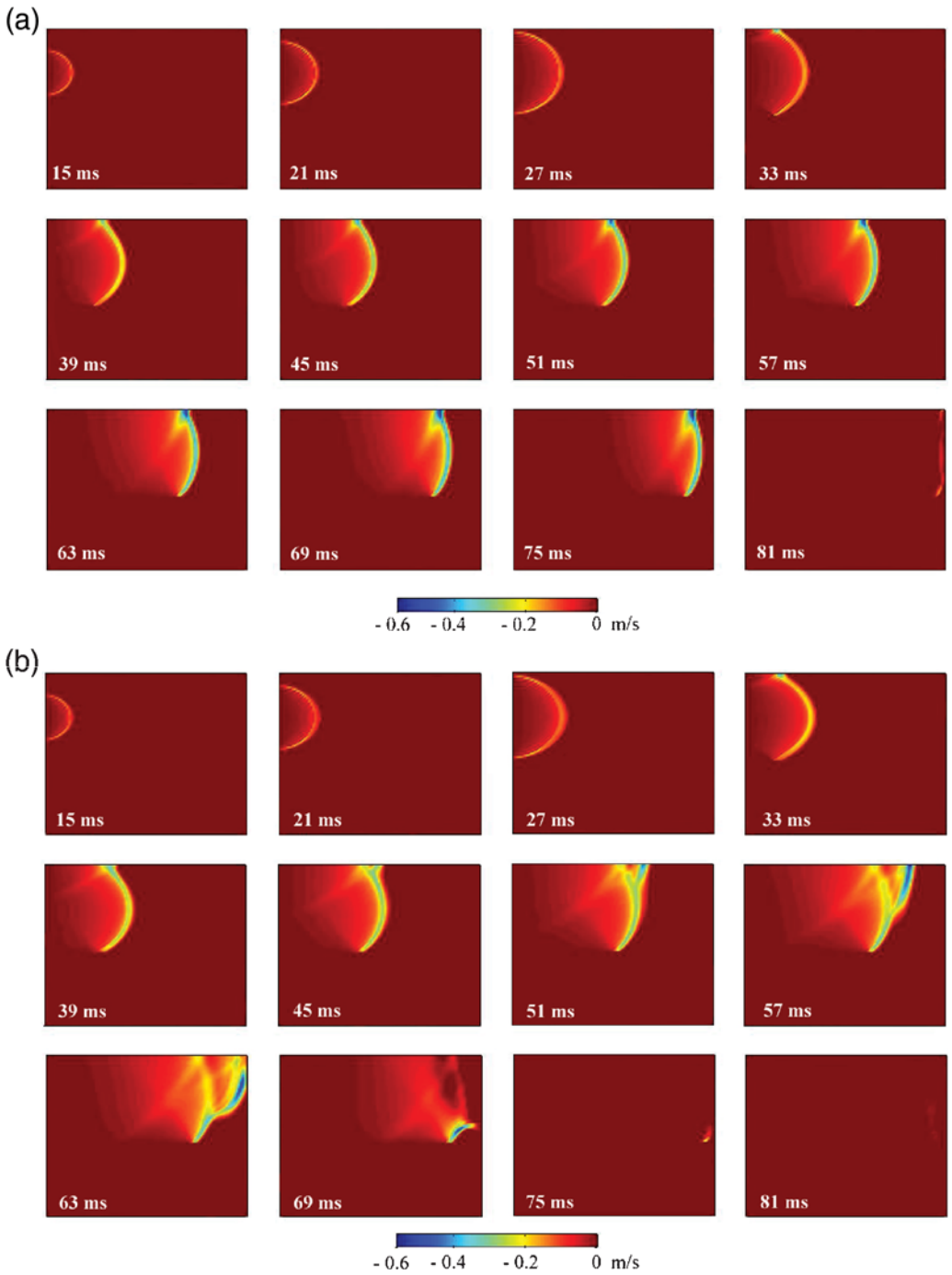

Figure 9. Snapshots of slip velocity (the component aligned with the prestress direction) in the fault plane, for (a) simulation 2 and (b) simulation 3. The former has sub-Rayleigh rupture velocity throughout. The latter undergoes the supershear transition between 39 and 45 msec, as evidenced by the emergence of the secondary rupture front from the free-surface intersection point of the sub-Rayleigh rupture. Each frame represents the entire fault plane, 2 m along strike (horiztonal), 1.83 m down-dip (vertical). Free surface is at the top; locking depth is halfway through the down-dip extent.

component for the foam events is shown in red, and the mean fault-normal component for the foam events is in blue (standard deviations, typically about 30%, are omitted from the plots for the sake of legibility). The fault-parallel component for the numerical simulation is represented by dashed black curves, and the fault-normal component is represented by black solid curves. The thin black curves represent the response spectrum for the numerical simulation in which the boundaries are located as in the foam model. The thick black curves represent the response spectrum for a numerical simulation identical to the first, except that the boundaries were extended beyond those of the foam model. The close agreement of the response spectra in those two cases confirms that boundary effects are not important to the analysis.

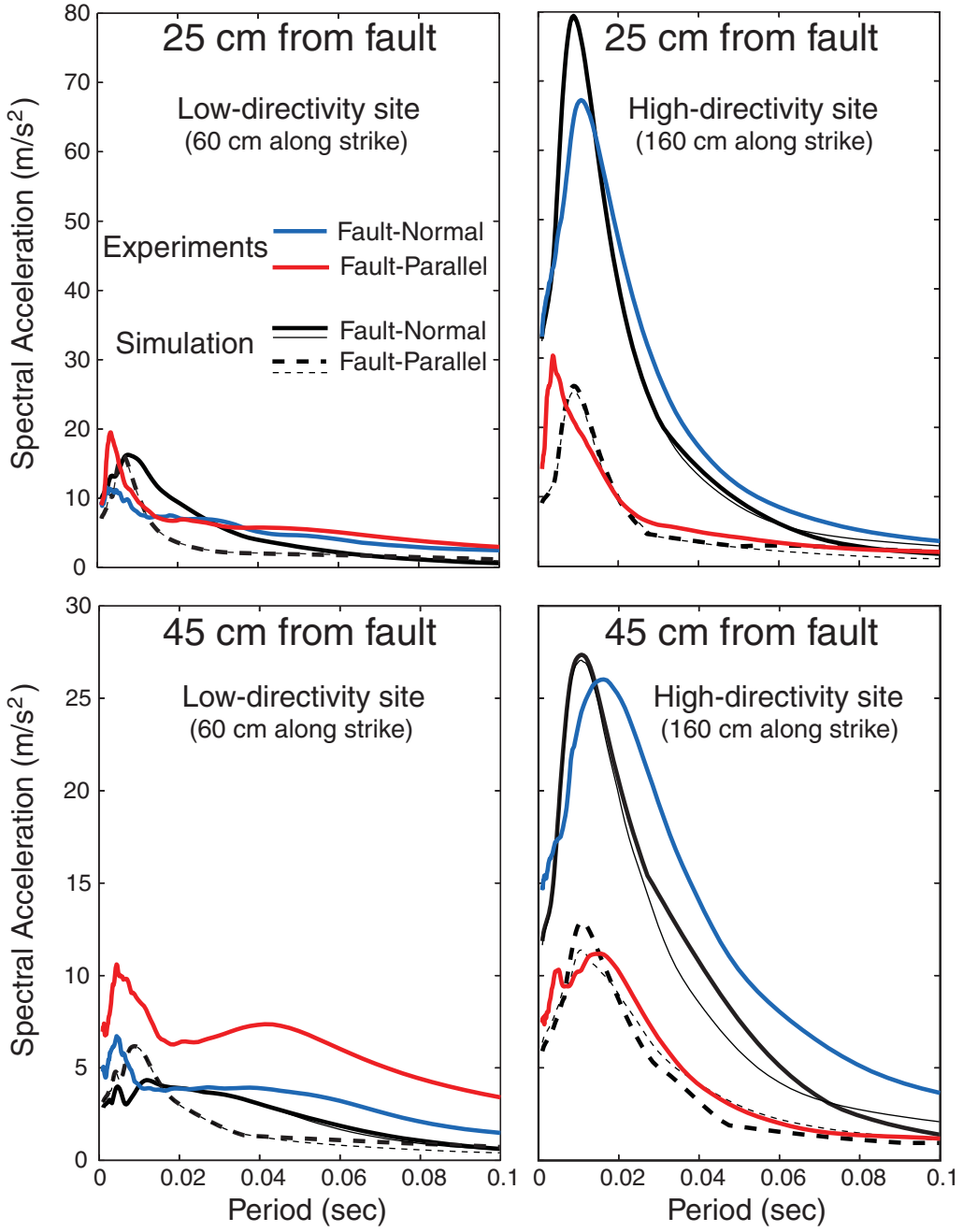

Figure 10. Mean response spectra for foam rubber experiments and numerical simulation 2. Experiments and simulation are for 320 Pa normal stress. The thick solid and dashed black curves are for a numerical simulation done with larger blocks, to delay the boundary reflections. (Along-strike distances [60 and 160 cm] refer to fault-parallel sensor; corresponding fault-normal sensors are actually at 55- and 155-cm distance, respectively.)

Analysis of Directivity

The fault-normal-component response spectra in Figure 10, at 25 cm from the fault trace, show strong directivity in both the foam and numerical simulations. There is a significant increase in peak spectral response as the distance along strike (away from the hypocenter) is increased, and the increase in the experimental response spectra is tracked well by that of the numerical simulation. Figure 10 also shows a large increase in the ratio of fault-normal to fault-parallel spectra in the along-strike direction, especially for the 25-cm profile. This trend in the fault-normal to fault-parallel spectral ratios is followed closely by the numerical simulation. Peak response of the fault-normal sensor located a distance of 155 cm along the fault trace occurs at a period of approximately 0.01 sec in both the numerical and foam models. The fault-normal peak response predicted by the numerical simulation (~80 m/sec^2) is slightly higher than the

mean of the foam experiments (~68 m/sec^2) at this sensor. The decay of the fault-normal spectra with distance from the fault (i.e., their change between the 25- and 45-cm distances) is reasonably well tracked by the numerical simulation, as is the distance decay of the fault-parallel component at the high-directivity sites. The fault-parallel component at the more distant (45 cm) low-directivity site is significantly underpredicted by the simulation, however, possibly reflecting a systematic difference in nucleation depth of the foam events relative to the numerical simulation (the low-directivity sites are relatively near the event epicenters).

Somerville *et al.* (1997) developed an empirical model for the effects of rupture directivity on earthquake response-spectral amplitudes. That model was derived from linear regression analysis of residuals (with respect to the regression model of Abrahamson and Silva, 1997), employing a function $X\cos(\theta)$ as a predictor variable for strike-slip events. The variable θ is the angle between the fault plane and the path from the epicenter to the site, and X is the fraction of the total rupture surface that lies between the epicenter and the site (Fig. 11). On simple theoretical considerations, one expects stronger forward directivity effects for smaller values of θ and for larger values of X, with maximum forward directivity when $X\cos(\theta)$ is equal to one. However, the majority of recording sites for earthquakes used in constructing this model are greater than 10 km from the fault. It is of interest to see how this model performs on the scale-model data set (and its numerical-model analogue), which provides many events with known rupture characteristics and extensive near-fault instrumental coverage.

We analyze the rupture propagation-induced directivity of the foam-model response spectra in a manner analogous to the Somerville *et al.* (1997) analysis of earthquake strong-motion records. Residuals were computed by removing the

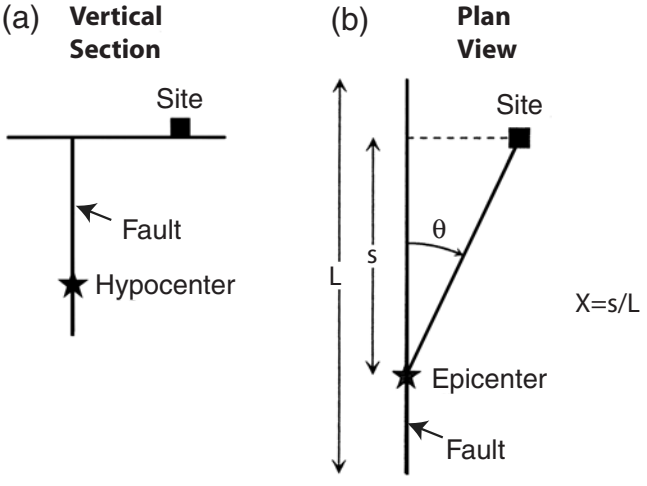

Figure 11. Definition of the predictor variable $X\cos(\theta)$ for seismic directivity from strike-slip earthquakes. The variable θ is the angle between the fault plane and the path from the epicenter to the site, and X is the fraction of the total rupture surface that lies between the epicenter and the site (from Somerville *et al.*, 1997).

mean effect of distance (measured to the nearest point on the fault-surface trace) from each horizontal-component spectral value. For each event, the mean of the natural logarithm of both fault-normal and fault-parallel spectral components at a distance of 25 cm from the fault was obtained. This value was then subtracted from the natural logarithm of each individual spectral value to obtain the residuals. This process was repeated for the horizontal-component spectral values at a distance of 45 cm from the fault. For each of a set of periods in the range of approximately 0.003–0.03 sec, residuals for all the 320 Pa normal-stress foam events were jointly fit to a regression line, with directivity function $X\cos(\theta)$ as the predictor variable. The same was done for spectral accelerations (at the corresponding recording locations) from simulation 2. Then the response-spectral periods T were expressed as nondimensional times $\tilde{T}$, where $\tilde{T} = T\beta/W$, $W = 1$ m, and $\beta = 36$ m/sec. That is, the nondimensional time gives the period in units of the S-wave transit time across the narrow dimension of the fault. Periods in the Somerville *et al.* empirical model were similarly scaled, using the representative values $W = 12$ km and $\beta = 3$ km/sec. It is worth bearing in mind, of course, that in both cases (experimental and empirical) we have substantial uncertainties in estimating an appropriate W.

Figure 12a–d compare the three resulting regression lines (for scale-model events, numerical simulation, and empirical model, respectively) at each of four periods (Gonzalez [2003] shows the full set of experimental residuals). The slopes (directivity slopes) are a measure of the strength of the forward directivity effect, and we summarize the slope information, as a function of nondimensional period, in Figure 12e. Standard errors of the directivity slopes are approximately 5% for the foam data set, 25% for the numerical-simulation, and 12% for the empirical model. At all periods shown, the slopes for the numerical and foam models are very similar, and almost statistically indistinguishable in the range $\tilde{T} \approx 0.4$–0.8. For periods shorter than about 0.4, the numerical model systematically overpredicts the experimental slopes by a small, but significant amount. This might be a reflection of some loss of coherence of the rupture front at small spatial scale in the experiments. Such loss of coherence is suggested by the presence, noted earlier, of an irregular component in the experimental waveforms at periods of a few milliseconds (5 msec corresponds to $\tilde{T} \approx 0.18$), and which is absent in the numerical simulation.

At periods comparable to the S transit time across the fault width, $\tilde{T} \approx 1$ (which may be near the upper limit at which the experimental spectra are meaningful, due to model boundary reflections), both experimental and simulation directivity slopes are also similar to slopes of the Somerville *et al.* empirical model. But for nondimensional periods shorter than about one, the experimental and numerical models systematically overpredict the empirical slopes, and with decreasing period the empirical slopes diverge systematically from the others. Some of this systematic decrease in directivity-slope ratio (empirical divided by experimental)

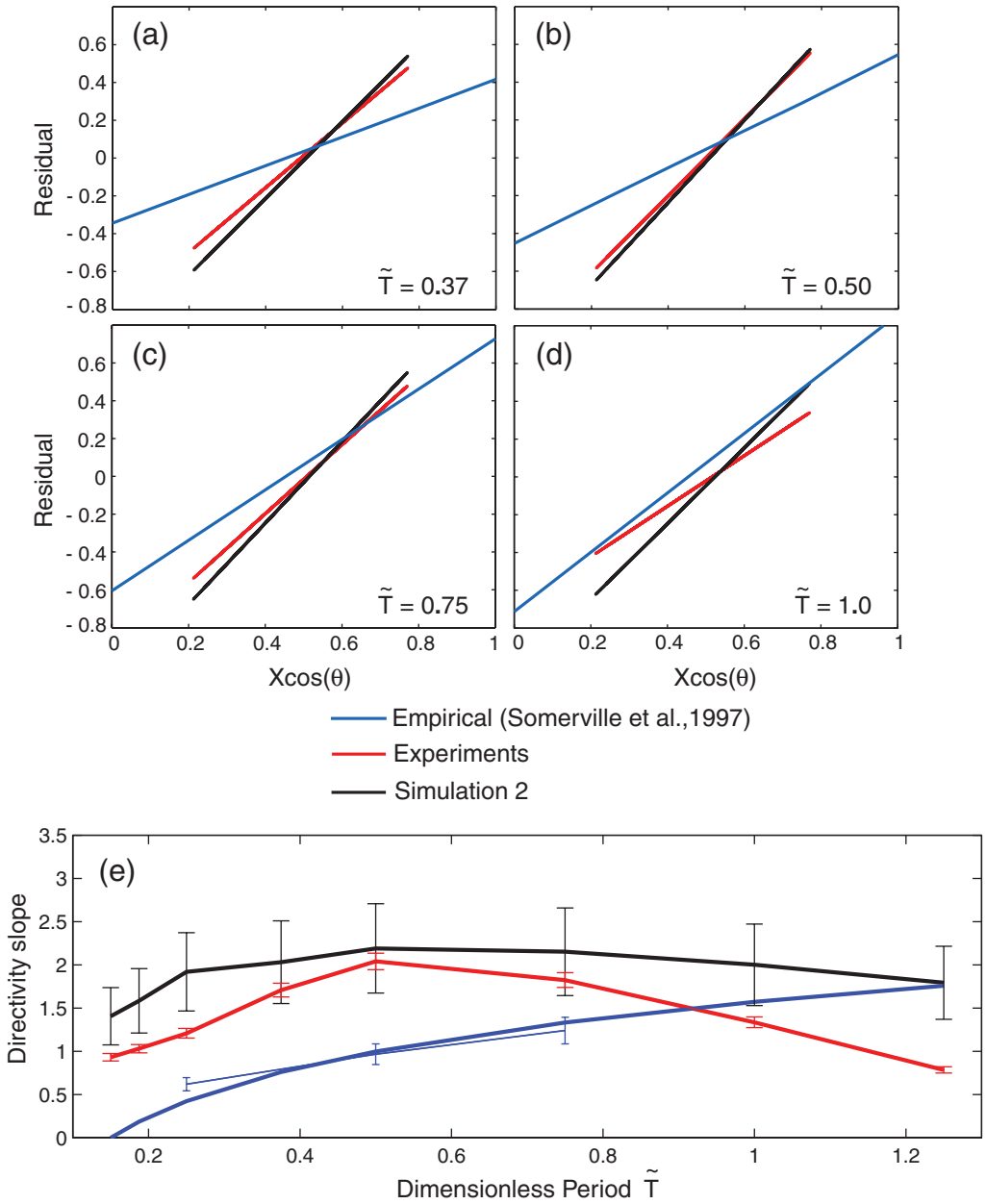

Figure 12. (a)–(d) Regression lines for scale-model experiments (red), numerical simulation (black), and empirical model (blue), respectively, at each of four periods. The predictor variable is $X\cos(\theta)$, and the response variable is the natural logarithm of the response-spectral ordinate. The period T has been scaled by the S-wave transit time across the fault width, that is, $\tilde{T} = T\beta/W$. (e) Plot of the regression slopes versus response-spectral period, with the same color representation as before for the experiments, numerical simulation, and empirical model, respectively. The thin blue line connects three single-period directivity-slope estimates obtained from the same data set from which the period-dependent Somerville *et al.* empirical model was derived.

with period may be a consequence of the greater rupture incoherence that we expect for natural earthquakes, compared with the experiments. Frictional parameters and/or the initial stresses acting in natural earthquakes are thought to be heterogeneous on a broad range of scales (the main evidence being the inferred heterogeneity of slip, e.g., Andrews, 1980, 1981; Mai and Beroza, 2002; Lavallée *et al.*, 2006), and this heterogeneity would be expected to induce incoherence in the rupture front over the same range of scales. Of course, the directivity decrease with period might also be explained in part by the heterogeneity of the propagation paths sampled by recordings of natural earthquakes.

Several recent studies have used residuals with respect to the empirical ground-motion models of the Next Generation Attenuation (NGA) project (e.g., Power *et al.*, 2006) to reassess near-fault directivity. It is difficult to compare these new empirical studies directly with the Somerville *et al.* (1997) model, as the new studies typically differ in record selection criteria (e.g., differing limits on the distance variable) and/or directivity parameterization (e.g., Abrahamson,

2000). Furthermore, some studies have found significant correlation between the directivity parameter and magnitude variable (e.g., Abrahamson and Silva, 2007), so that some of the directivity effect may become subsumed in the magnitude scaling in the NGA models. However, two generalizations are supported by these studies, albeit provisionally: (1) At dimensionless periods $\tilde{T}$ of order 1 (which scales to ~4 sec), there is convincing evidence in the NGA residuals for a directivity effect for strike-slip earthquakes, representable (though imperfectly) by $X\cos\theta$, and within roughly a factor of 2 in amplitude of the effect predicted by the Somerville *et al.* model. For example, at a periods of both 3 and 5 sec, Abrahamson and Silva find a shift of ~0.5 natural log units between averages of residuals taken over the two ranges $0 < X\cos\theta < 0.1$ and $0.4 < X\cos\theta < 1.0$, roughly half the value that would be predicted for these averages as constructed from the Somerville *et al.* empirical model (and, absent a single, very large outlier from the 1999 Duzce earthquake, the factor of 2 difference disappears and the directivity-slope estimates from the Abrahamson and Silva residuals would remain very close to the Somerville *et al.* estimates at these periods). Similarly, at a 3 sec period ($\tilde{T} \sim 0.75$ with our scaling), Spudich and Chiou (2006) find that $X\cos\theta$ works as a predictor for NGA residuals (for large strike-slip earthquakes), and Watson-Lamprey (2007) estimate a directivity slope of ~0.5 in residuals relative to the NGA model of Abrahamson and Silva (2007), about a factor of 2 smaller than the corresponding Somerville *et al.* estimate. (2) At periods $\tilde{T}$ significantly less than 1, the NGA residuals show directivity declining with period, and the weight of the evidence so far seems to indicate an even more rapid decrease with period than predicted by the Somerville *et al.* model. For example, Spudich and Chiou (2006) and Watson-Lamprey (2007) find no significant directivity in NGA residuals at 1 sec ($\tilde{T} \sim 0.25$) and Abrahamson and Silva report no significant effect at 1.5 sec ($\tilde{T} \sim 0.4$).

The suggestion that rupture incoherence contributes to the short-period decrease in directivity of natural earthquakes, relative to the experiments and numerical model, requires further comment, because a short-period diminution of directivity is absent in some kinematic models of heterogeneous rupture. For example, Boore and Joyner (1978) and Joyner (1991) analyzed directivity from unilateral, one-dimensional rupture in the far-field approximation, under the assumption that rupture velocity is everywhere positive and subshear. More precisely, the idealization was that the slip-rate function $\dot{s}(x,t)$ factors as $q(x)h[t - x/v(x)]$, where q has support interval $[0, L]$, and $0 < v(x) < \beta$, so that rupture time is a monotonic function of x. In this monotonic-rupture model, rupture complexity can take the form of along-strike variations in both total slip $q(x)$ and local rupture velocity $v(x)$. Following Joyner, we first consider slip variations alone. The far-field displacement amplitude spectrum $|U(\omega)|$ from such a source is proportional to the wavenumber spectrum of q, in the form

$$|U(\omega)| \propto |H(\omega)||\bar{Q}(\omega)|, \tag{22}$$

where

$$\bar{Q}(\omega) = Q[v^{-1}(1 - v\cos\theta/\beta)\omega] \tag{23}$$

in which H and Q are the Fourier transforms of h and q, respectively, and θ is the angle between the source-to-receiver direction and the rupture propagation direction (Joyner, 1991). Thus, the forward directivity effect amounts to a shift toward higher frequencies of the spectrum $\bar{Q}(\omega)$. As Joyner (1991) points out, if the spectrum $Q(k)$ is proportional to k^{-p} at a large wavenumber, this shift amounts to a high-frequency spectral enhancement by the factor $(1 - v\cos\theta/\beta)^{-p}$,

$$|U(\omega)| \propto [|H(\omega)|(\omega/v)^{-p}](1 - v\cos\theta/\beta)^{-p} \tag{24}$$

and there is no high-frequency cutoff to the directional enhancement. Boore and Joyner (1978) further show by numerical simulations that adding complexity in the form of rupture-velocity variations does not alter this conclusion (v in equation 24 is then interpreted as the mean rupture velocity). The latter result is a consequence of the fact that individual rupture segments all occur unilaterally in this idealization: a rupture segment of length ΔL, with rupture duration $\Delta L/v(x)$, will radiate a pulse in direction θ with duration $[1 - v(x)\cos\theta/\beta]\Delta L/v(x)$ and amplitude proportional to $[1 - v(x)\cos\theta/\beta]^{-1}$, so individual pulse contributions are compressed in the forward directivity direction by the same factor (on average) as is the overall envelope of the displacement time history.

However, the conclusion changes if we relax the monotonic-rupture conditions and instead model rupture complexity in a form that permits rupture to be omnidirectional at small length scales, even though unidirectional at large scales. Numerical simulations of rupture in the presence of spatial variations of frictional strength and/or initial stress frequently suggest just such a behavior. Slip often jumps ahead of the main rupture front at some points to create a secondary rupture front that moves in all directions until it coalesces with the main, advancing front (e.g., Day, 1982b; Olsen *et al.*, 1997). Conversely, strong patches are sometimes left unbroken by the main front, then break inward from all directions (e.g., Das and Kostrov, 1983), finally emitting outward-propagating interface waves that drive secondary, damped slip pulses on previously ruptured parts of the fault surface (e.g., Dunham *et al.*, 2003; Dunham, 2005). Rupture complexity of this type may be quite difficult to parameterize effectively in a purely kinematic model description, yet it can have important consequences for ground-motion excitation (e.g., Olsen *et al.*, 2008).

We can get a rough idea of the effect that rupture complexity of this sort has on high-frequency directivity by considering an idealization (similar to the Zeng *et al.* [1994] composite model) in which the rupture takes the form of

a large-scale front traveling unilaterally at constant velocity v, triggering slip subevents upon its arrival at points with x coordinates x_j, $j = 1, \ldots, N$. The x_j are independent random variables with common probability density $f(x_j)$, where f has support interval $[0, L]$. The far-field displacement field (at some fixed reference distance) from the jth subevent has Fourier transform (at frequency ω) given by complex random variable $\Omega_j(\omega)$. We will assume that the Ω_j are identically distributed, the expected value of the energy spectrum, $E[\Omega_j(\omega), \Omega_j^*(\omega)]$, having a common value $\Omega^2(\omega)$ for all subevents, and the interevent coherency, $E[\Omega_j(\omega), \Omega_k^*(\omega)]/\Omega(\omega)^2$, $j \neq k$, having the common value $C(\omega)$ for all subevent pairs. We further assume that the slip subevents have sufficient directional variability that there is no dependence of the spectral moments Ω^2 and C on azimuthal coordinate θ (apart from the double-couple radiation pattern, which we suppress here, as is done in Joyner, 1991). Then the total radiated energy spectrum from the subevents is

$$UU^* = \left[\sum_{j=1}^{N} \Omega_j(\omega) e^{-i\omega/v(1-v\cos\theta/\beta)x_j}\right] \times \left[\sum_{k=1}^{N} \Omega_k^*(\omega) e^{i\omega/v(1-v\cos\theta/\beta)x_k}\right]. \quad (25)$$

The expected value is

$$E(UU^*) = E\left\{\left[\sum_{j=1}^{N} \Omega_j(\omega) e^{-i\omega/v(1-v\cos\theta/\beta)x_j}\right] \times \left[\sum_{k=1}^{N} \Omega_k^*(\omega) e^{i\omega/v(1-v\cos\theta/\beta)x_k}\right]\right\}, \quad (26)$$

and the summation can be carried out in a manner similar to the subevent summation of Joyner and Boore (1986, appendix). The result is

$$E(UU^*) = N\Omega^2(\omega)[1 + (N-1)C(\omega)\bar{F}(\omega)\bar{F}^*(\omega)], \quad (27)$$

where

$$\bar{F}(\omega) = F[v^{-1}(1 - v\cos\theta/\beta)\omega] \quad (28)$$

and F is the Fourier transform of the density function $f(x)$.

We can simplify by considering identical slip events, in which case $C(\omega) = 1$. Then, assuming the spectrum $F(k)$ of the density function is proportional to k^{-p} for a wavenumber large compared with $1/L$, the second term dominates (27) for $\omega L/v \ll (N-1)^{1/2p}$, so for $1 \ll \omega L/v \ll (N-1)^{1/2p}$ we have

$$E(UU^*) \approx N(N-1)\Omega^2\bar{F}(\omega)\bar{F}^*(\omega). \quad (29)$$

Then, by virtue of the frequency shift (28), the amplitude spectrum acquires the same directivity factor as we had in (24) for the monotonic-rupture model,

$$\sqrt{E(\tilde{U}\tilde{U}^*)} \propto \left[\sqrt{N(N-1)}\Omega(\omega)\left(\frac{v}{\omega L}\right)^p\right] \times (1 - v\cos\theta/\beta)^{-p}, \quad \text{for } 1 \ll \omega L/v \ll (N-1)^{1/2p}. \quad (30)$$

For $\omega L/v \gg (N-1)^{1/2p}$, however, the first term dominates, so there is a high-frequency cutoff of directivity,

$$\sqrt{E(\tilde{U}\tilde{U}^*)} \propto \sqrt{N}\Omega(\omega), \quad \text{for } \omega L/v \gg (N-1)^{1/2p} \quad (31)$$

(and, in general, $C(\omega)$ will be less than 1 at frequencies above the subevent corner frequency, further promoting the high-frequency directivity cutoff). Thus, this form of rupture complexity, in which a component of nonmonotonic rupture is present at small scales, may be a contributor to the short-period diminution of directivity found by Somerville *et al.* (1997).

Conclusions

Scale-model earthquakes in foam rubber propagate with terminal rupture velocity approaching the Rayleigh velocity of the medium, have cracklike slip-velocity waveforms (i.e., slip duration at a point is of the order of the narrower fault dimension W divided by the S wave speed β), and exhibit near-fault ground motion strongly enhanced along strike by rupture-induced directivity. Most features of the experimental waveforms, including the initiation time, shape, duration, and absolute amplitude of the main acceleration pulses, are successfully reproduced by a numerical model. The acceleration pulses in the experimental and numerical models show similar decay with distance away from the fault, and the fault-normal components in both models show similar, large amplitude growth with increasing distance along fault strike. Likewise, the fault-normal spectral response peak (at period $\sim W/3\beta$) increases approximately sixfold along strike, on average, in the experiments, with similar increase (about fivefold) in the corresponding numerical simulation. Although there is no definitive evidence of supershear rupture velocity in the experimental records, relatively small parameter changes induce a supershear rupture transition in the numerical model. The transition, when it occurs, is driven by the reflected slip pulse generated at the free-surface breakout of rupture.

The experimental- and numerical-model response spectra are in good agreement with the Somerville *et al.* (1997) empirical directivity model for natural earthquakes at long periods (periods near $\sim W/\beta$). This agreement suggests that, despite the limited near-fault data available to constrain the empirical model, it successfully represents the large-scale dynamics controlling directivity. At shorter periods, both

foam and numerical models overpredict directivity effects relative to the empirical model. The amount of overprediction increases systematically with diminishing period, as would be expected if the difference were due to fault-zone heterogeneities in stress, frictional resistance, and elastic properties. These complexities, present in the Earth but absent or minimal in the foam model (and in numerical simulations of the foam model), can be expected to reduce rupture-front and wavefront coherence, likely accounting at least in part for the reduced short-period directivity of the empirical model relative to the scale-model events. Realistic rupture-front incoherence may induce a significant component of nonmonotonicity in along-strike rupture times, and the resulting fault behavior may be challenging to parameterize kinematically.

Acknowledgments

We thank Paul Somerville for supplying data from his empirical study of seismic directivity, as well as for providing a helpful review of the manuscript. We also thank David Oglesby and Pengcheng Liu for their helpful reviews. This work was supported by the Pacific Earthquake Engineering Research (PEER) Center Lifelines Program, Projects 1D02, by the National Science Foundation (NSF) under Grant Number ATM-0325033, and by the Southern California Earthquake Center (SCEC). SCEC is funded by NSF Cooperative Agreement EAR-0529922 and U.S. Geological Society (USGS) Cooperative Agreement 07HQAG0008. The SCEC contribution number for this article is 1111.

References

Aagaard, B. T., T. H. Heaton, and J. F. Hall (2001). Dynamic earthquake ruptures in the presence of lithostatic normal stresses: implications for friction models and heat production, *Bull. Seismol. Soc. Am.* **91,** no. 6, 1765–1796.

Abercrombie, R. E., and J. R. Rice (2005). Can observations of earthquake scaling constrain slip weakening?, *Geophys. J. Int.* **162,** 406–424, doi 10.1111/j.1365-246X.2005.02579.x.

Abrahamson, N. A. (2000). Effects of rupture directivity on probabilistic seismic hazard analysis, in *Proc. Sixth International Conference on Seismic Zonation*, Palm Springs, California. 12–15 November 2000.

Abrahamson, N. A., and W. J. Silva (1997). Empirical response spectral attenuation relations for shallow crustal earthquakes, *Seism. Res. Lett.* **68,** 94–127.

Abrahamson, N. A., and W. J. Silva (2007). NGA ground motion relations for the geometric mean horizontal component of peak and spectral ground motion parameters, a report for the Pacific Earthquake Engineering Research Center.

Anderson, J. C., and V. V. Bertero (1987). Uncertainties in establishing design earthquakes, *J. Struct. Eng.* **113,** 1709–1724.

Andrews, D. J. (1976), Rupture propagation with finite stress in antiplane strain, *J. Geophys. Res.* **81,** 3575–3582.

Andrews, D. J. (1980). A stochastic fault model, I, Static case, *J. Geophys. Res.* **85,** 3867–3877.

Andrews, D. J. (1981). A stochastic fault model, II, Time-dependent case, *J. Geophys. Res.* **86,** 10,821–10,834.

Archuleta, R. J. (1984). A faulting model for the 1979 Imperial Valley earthquake, *J. Geophys. Res.* **89,** 4559–4585.

Archuleta, R. J., and S. H. Hartzell (1981). Effects of fault finiteness on near-source ground motion, *Bull. Seismol. Soc. Am.* **71,** 939–957.

Boore, D. M., and W. B. Joyner (1978). The influence of rupture incoherence on seismic directivity, *Bull. Seismol. Soc. Am.* **68,** 283–300.

Bouchon, M., and M. Vallee (2003). Observation of long supershear rupture during the magnitude 8.1 Kunlunshan earthquake, *Science* **301,** no. 5634, 824–826.

Bouchon, M., M. P. Bouin, H. Karabulut, M. N. Toksoz, M. Dietrich, and A. Rosakis (2001). How fast is rupture during an earthquake? New insights from the 1999 Turkey earthquakes, *Geophys. Res. Lett.* **28,** 2723–2726.

Bouchon, M., H. Sekiguchi, K. Irikura, and T. Iwata (1998). Some characteristics of the stress field of the 1995 Hyongo-ken Nanbu (Kobe) earthquake, *J. Geophys. Res.* **103,** 24,271–24,282.

Brune, J. N., and A. Anooshehpoor (1998). A physical model of the effect of a shallow weak layer on strong motion for strike-slip ruptures, *Bull. Seismol. Soc. Am.* **88,** 939–957.

Das, S., and B. V. Kostrov (1983). Breaking of a single asperity: rupture process and seismic radiation, *J. Geophys. Res.* **88,** 4277–4288.

Day, S. M. (1982a). Three-dimensional finite difference simulation of fault dynamics: rectangular faults with fixed rupture velocity, *Bull. Seismol. Soc. Am.* **72,** 705–727.

Day, S. M. (1982b). Three-dimensional simulation of spontaneous rupture: the effect of nonuniform prestress, *Bull. Seismol. Soc. Am.* **72,** 1881–1902.

Day, S. M. (1991), Numerical simulation of fault propagation with interface separation(abstract), *Trans. AGU* **72,** 486.

Day, S. M., and G. P. Ely (2002). Effect of a shallow weak zone on fault rupture: numerical simulation of scale-model experiments, *Bull. Seismol. Soc. Am.* **92,** 3022–3041.

Day, S. M., L. A. Dalguer, N. Lapusta, and Y. Liu (2005). Comparison of finite difference and boundary integral solutions to three-dimensional spontaneous rupture, *J. Geophys. Res.* **110,** B12307, doi 10.1029/2005JB003813.

DiToro, G., D. L. Goldsby, and T. E. Tullis (2004). Friction falls towards zero in quartz rock as slip velocity approaches seismic rates, *Nature* **47,** 436–439.

Dunham, E. M. (2005). Dissipative interface waves and the transient response of a three-dimensional sliding interface with Coulomb friction, *J. Mech. Phys. Solids* **53,** 327–357, doi 10.1016/j.jmps.2004.07.003.

Dunham, E. M. (2007). Conditions governing the occurrence of supershear ruptures under slip-weakening friction, *J. Geophys. Res.* **112,** B07302, doi 10.1029/2006JB004717.

Dunham, E. M., and R. J. Archuleta (2004). Evidence for a supershear transient during the 2002 Denali fault earthquake, *Bull. Seismol. Soc. Am.* **94,** S256–S268.

Dunham, E. M., P. Favreau, and J. M. Carlson (2003). A supershear transition mechanism for cracks, *Science* **299,** 1557–1559.

Goldsby, D. L., and T. E. Tullis (2002), Low frictional strength of quartz rocks at subseismic slip rates, *Geophys. Res. Lett.* **29,** 1844, doi 10.1029/2002GL015240.

Gonzalez, S. H. (2003). Foam rubber and numerical simulations of near-fault seismic directivity, *Master's Thesis*, San Diego State University, San Diego, California.

Guatteri, M., and P. Spudich (2000). What can strong-motion data tell us about slip-weakening fault-friction laws?, *Bull. Seismol. Soc. Am.* **90,** 98–116.

Hall, J. F., T. H. Heaton, M. W. Halling, and D. J. Wald (1995). Near-source ground motion and its effects on flexible buildings, *Earthq. Spectra* **11,** 569–605.

Ida, Y. (1972). Cohesive force across the tip of a longitudinal-shear crack and Griffith's specific surface energy, *J. Geophys. Res.* **77,** 3796–3805.

Ide, S., and M. Takeo (1997). Determination of constitutive relations of fault slip based on seismic waves analysis, *J. Geophys. Res.* **102,** 27,379–27,391.

Joyner, W. B. (1991). Directivity for nonuniform ruptures, *Bull. Seismol. Soc. Am.* **81,** 1391–1395.

Joyner, W. B., and D. M. Boore (1986). On simulating large earthquake by Green's-function addition of smaller earthquakes, in *Earthquake*

Source Mechanics, S. Das, J. Boatwright and C. H. Scholz (Editors), American Geophysical Monograph **37**, 269–274.

Kaneko, Y., N. Lapusta, and J-P. Ampuero (2007). Spectral element modeling of dynamic rupture and long-term slip on rate and state faults (abstract), *Annual Meeting of Southern California Earthquake Center (SCEC), Proceedings and abstracts* 8–12 September 2007, Palm Springs, California, 130 pp.

Lavallée, D., P. Liu, and R. J. Archuleta (2006). Stochastic model of heterogeneity in earthquake slip spatial distributions, *Geophys. J. Int.* **165,** 622–640, doi 10.1111/j.1365-246X.2006.02943.x.

Madariaga, R., K. B. Olsen, and R. J. Archuleta (1998). Modeling dynamic rupture in a 3-D earthquake fault model, *Bull. Seismol. Soc. Am.* **88,** 1182–1197.

Mai, P. M., and G. C. Beroza (2002). A spatial random field model to characterize complexity in earthquake slip, *J. Geophys. Res.* **107,** 2308, doi 10.1029/2001JB000588.

Mikumo, T., K. B. Olsen, E. Fukuyama, and Y. Yagi (2003). Stress-breakdown time and slip-weakening distance inferred from slip-velocity functions on earthquake faults, *Bull. Seismol. Soc. Am.* **93,** 264–282.

Olsen, K. B., S. M. Day, J. B. Minster, Y. Cui, A. Chourasia, D. Okaya, P. Maechling, and T. Jordan (2007). TeraShake2: spontaneous rupture simulations of M_w 7.7 earthquakes on the southern San Andreas fault, *Bull. Seismol. Soc. Am.* **98**, 1162–1185.

Olsen, K. B., R. Madariaga, and R. J. Archuleta (1997). Three dimensional dynamic simulation of the 1992 Landers earthquake, *Science* **278,** 834–838.

Palmer, A. C., and J. R. Rice (1973), The growth of slip surfaces in the progressive failure of overconsolidated clay slopes, *Proc. R. Soc. Lond. A* **332,** 537.

Power, M., B. Chiou, N. Abrahamson, and C. Roblee (2006). The next generation of ground motion attenuation models (NGA) project: an overview, *Proc. Eighth National Conf. Earthquake Engineering*, paper no. 22.

Somerville, P. G., N. F. Smith, R. W. Graves, and A. Abrahamson (1997). Modification of empirical strong ground motion attenuation relations to include the amplitude and duration effects of rupture directivity, *Seism. Res. Lett.* **68,** 199–222.

Spudich, P., and B. S. J. Chiou (2006). Directivity in preliminary NGA residuals, Final Project Report for PEER Lifelines Program Task 1M01, Subagreement SA5146-15811, 37 pp.

Tinti, E., P. Spudich, and M. Cocco (2005). Earthquake fracture energy inferred from kinematic rupture models on extended faults, *J. Geophys. Res.* **110,** B12303, doi 10.1029/2005JB003644.

Watson-Lamprey, J. (2007). In search of directivity (abstract), *Seism. Res. Lett.* **78,** 273.

Zeng, Y., J. G. Anderson, and G. Yu (1994). A composite source model for computing realistic synthetic strong ground motions, *Geophys. Res. Lett.* **21,** 725–728.

Department of Geological Sciences
San Diego State University
San Diego, California 92182
(S.M.D.)

U.S. Nuclear Regulatory Commission
Rockville, Maryland 20852-2738
(S.H.G.)

Seismological Laboratory
University of Nevada
Reno, Nevada 89557
(R.A., J.N.B.)

Manuscript received 26 July 2007